Challenge Journal of
CONCRETE RESEARCH LETTERS

Vol.14 No.1 (2023)

absorption aerated concrete artificial neural network

compressive strength concrete corrosion

cracking curing ductility durability energy

absorption ferrocement flexural strength

fly ash fracture mechanics mechanical properties

mortar nanoparticle reinforced concrete

self- compacting concrete steam curing

strengthening superplasticizer tensile strength

workability waste disposal water a tion

ISSN 2548-0928

TULPAR
ACADEMIC PUBLISHING

Challenge Journal of Concrete Research Letters

EDITOR IN CHIEF

Prof. Dr. Mohamed Abdelkader ISMAIL	*Miami College of Henan University, China*

EDITORIAL BOARD

Prof. Dr. Ashraf Ragab MOHAMED	*Alexandria University, Egypt*
Prof. Dr. Ayman NASSIF	*University of Portsmouth, United Kingdom*
Prof. Dr. Gamal Elsayed ABDELAZIZ	*Benha University, Egypt*
Prof. Dr. Han Seung LEE	*Hanyang University, Republic of Korea*
Prof. Dr. Zubair AHMED	*Mehran University, Pakistan*
Prof. Dr. Jiwei CAI	*Henan University, China*
Assoc. Prof. Dr. Meral OLTULU	*Atatürk University, Turkey*
Assoc. Prof. Dr. Saleh Omar BAMAGA	*University of Bisha, Saudi Arabia*
Dr. Aamer Rafique BHUTTA	*The University of British Columbia, Canada*
Dr. Khairunisa MUTHUSAMY	*Universiti Malaysia Pahang, Malaysia*
Dr. Mahmoud SAYED AHMED	*Ryerson University, Canada*
Dr. Jitendra Kumar SINGH	*Hanyang University, Republic of Korea*
Dr. Türkay KOTAN	*Erzurum Technical University, Turkey*

E-mail: *cjcrl@challengejournal.com*

Web page: *cjcrl.challengejournal.com*

TULPAR Academic Publishing
www.tulparpublishing.com

Challenge Journal of Concrete Research Letters

CONTENTS

Research Articles

Case Studies

TULPAR ACADEMIC PUBLISHING

Challenge Journal of Concrete Research Letters

Research Article

Axial compression behaviour of concrete-filled auxetic tubular short columns

Kemal Solak [a], Suleyman Nazif Orhan [a,*]

[a] *Department of Civil Engineering, Erzurum Technical University, 25050 Erzurum, Türkiye*

ABSTRACT

Concrete-filled steel columns (CFSCs) are of great interest in the literature as they are capable of carrying higher loads by combining the exceptional qualities of steel and concrete. With auxetic materials being introduced to civil engineering applications, the influence of these materials on CFSCs remains a matter of curiosity. The current study implements a nonlinear finite element analysis to evaluate the performance of circular CFSCs with six auxetic tubes under axial compression and the proposed numerical model was validated using published experimental data. The effect of the auxetic steel tube's porosity and Poisson's ratio on CFSCs was examined parametrically in terms of ultimate strength using the confined concrete model. Moreover, the stress distributions of the concrete and the auxetic steel tubes were also thoroughly examined. Based on the findings of the analysis, the ultimate load of CFSCs, utilising auxetic tubes with the same density and porosity but different Poisson's ratio, increased proportionally with the increase of auxetic behaviour. When it comes to auxetic tubes with different densities and porosities, the influence of the Poisson's ratio of the tubes diminished and the stiffness of tubes became more dominant over the mechanical characteristics of columns as the density of the auxetic steel tubes increased or decreased. The stiffness of the auxetic tubes reduced as porosity increased, as did the ultimate load of the columns. Additionally, the ultimate loads of the auxetic steel tube columns are found to be lower than those of bare steel tube columns filled with concrete due to perforations.

ARTICLE INFO

Article history:
Received 1 November 2022
Revised 27 November 2022
Accepted 20 December 2022

Keywords:
Concrete-filled steel columns
Auxetic tube
Confined concrete model
Axial load
Numerical analysis

1. Introduction

In modern structural industries, novel composites are continually being developed and investigated to enhance conventional structures' properties (Lacki et al. 2018; Gao et al. 2020). Steel-concrete composite columns are the most frequently encountered composite structures and many studies have previously demonstrated the benefits of employing steel-concrete composite columns in civil engineering (Soliman et al. 2013; Duarte et al. 2016). Concrete-filled steel composite columns are a type of steel-concrete composite and take advantage of concrete's excellent compression properties and steel's high tensile strength to exhibit superiority over conventional bare steel columns and reinforced concrete columns (Ellobody and Young 2011; Lacki et al. 2021). The confinement of the concrete core by a steel tube leads to a tri-axial state of compressive stresses, which improves the energy absorption, strength and ductility of the concrete. Moreover, the concrete infill prevents inward local buckling of the steel tube to a certain extent, thereby increasing the axial load capacity and buckling resistance of steel confined concrete columns (Hassanein et al. 2013; Gupta and Singh 2014; Ma et al. 2019). Even though many cross-sections of steel tubes can be used such as circular, elliptical, square, polygonal, and rectangular in concrete-filled steel columns, circular tubes provide the greatest confinement to the core of concrete by evenly dispersing stresses along the inward wall of the tube (Tao and Han 2006; Liang and Fragomeni 2009; Zha

* *Corresponding author*. Tel.: 444-5-388 ; Fax: +90-442-230-0036 ; E-mail address: s.orhan@erzurum.edu.tr (S. N. Orhan)
ISSN: 2548-0928 / DOI: https://doi.org/10.20528/cjcrl.2023.01.001

et al. 2013; Wang et al. 2022). The performance of circular concrete-filled steel columns (CFSC) under varied loading situations has been examined experimentally and numerically by researchers. Schneider (1998) conducted an experimental and analytical study to investigate the mechanical performance of compression loaded concrete-filled circular and rectangular steel tubes. The confinement of the concrete, as well as the effect of the steel tube cross section and the wall thickness of tubes on the ultimate strength were addressed in this study. Huang et al. (2002) studied the parametric analysis of concrete-filled columns with and without tie bars in terms of ultimate strength and ductility utilising circular and square cross-sections, both experimentally and numerically. Giakoumelis and Lam (2004) investigated high strength concrete-filled circular short columns under compression loading while revealing the effect of steel tube thickness, bond strength at the interface and confinement of the concrete core. They compared experimental values with different existing codes and suggested a coefficient to be used in codes to evaluate the influence of concrete confinement. Yu et al. (2008) attempted to investigate the feasibility of combining tubular steel columns with high strength concrete. In the experiments, specimens with varying cross-sections, slenderness ratios, and eccentricity loads were employed. As seen in the above studies, the steel tube's confinement effect has a major impact on the axial load capacity, which is mostly investigated (De Oliveira et al. 2010). Researchers investigated the confinement effect utilising spiral reinforcement (Kim et al. 2020) and steel rings (Lai and Ho 2014) due to the lack of perfect confinement of the bare steel tube.

Auxetic structures, which have a negative Poisson's ratio, are worth investigating with their exceptional features in various fields. Different geometric shapes and designs of auxetic structures have been offered in the literature to enhance their mechanical performance (Orhan and Erden 2022a, 2022b). One of the most common geometric shapes in auxetics is tubular structures. Because of their energy absorption capabilities, shear resistance, and bending resistance, auxetic tubulars are the most suitable structures for multidisciplinary studies. Ren et al. (2016) investigated the performance of buckling-induced auxetics experimentally and numerically in 3D tubular form under tension and compression states. Munib et al. (2015) fabricated a novel polymeric auxetic bone stent and investigated the mechanical character and deformation behaviour to assist alleviation of some of the current issues with bone internal fixation systems. Ren et al. (2022) experimentally examined the stiffness and energy absorption ability of foam-filled auxetic tubulars and compared results with finite element analysis. It has been observed that the interaction between the two materials is improved by transferring the axial load as lateral pressure to the inner wall of the tube. Solak and Orhan (2023) proposed a novel methodology to modify peanut-shaped auxetic tubular structures by rotating the unit cells by an angle and placing a stiffener at the exact centre of the peanut perforations. In this study, peanut-shaped tubular structures were numerically investigated and it was revealed that when stiffeners are used, high auxetic behaviour and high stiffness can coexist. Luo et al. (2022) utilised auxetic, non-auxetic, and bare steel tubes to generate concrete-filled composites. In this study, a new methodology was presented to improve the interface bonding between concrete and steel, local buckling of the steel tube and insufficient confinement of concrete.

Concrete-filled auxetic steel columns (CFASC) clearly appear to be leading a new trend in the literature. In the above study (Luo et al. 2022), it was demonstrated that employing the auxetic tube increased the confinement effect of concrete, and the findings were promising when compared to the non-auxetic encasement. The lack of studies in the literature on the mechanical behaviour of CFASCs with different Poisson's ratios and porosities has led to such a need. Therefore, in this study, it is aimed to adapt peanut-shaped perforated auxetic steel tubular structures to CFSCs to perform parametric analysis by using the finite element method. The mechanical character of the columns was examined under compression according to different parameters. Three distinct models with the same porosity, different negative Poisson's ratios and three models with different porosities were investigated and the findings were compared in terms of ultimate strength.

2. Materials and Method

2.1. Material properties of confined concrete

Since the column is loaded axially, the concrete infill expanded laterally and was restricted by the exterior steel tube. This confinement causes an increase in the strength and ductility of the concrete (Zhang et al. 2019), as shown in Fig. 1. Based on existing literature (Kedziora and Anwaar 2019), the constitutive stress-strain relationship and relevant parameters of confined concrete were derived by adapting the Drucker-Prager plasticity model.

For circular sections enclosed by steel tubes, Mander et al. (1988) proposed the following equation:

$$f'_{cc} = f'_{co} \cdot \left(-1.254 + 2.245 \cdot \left(\sqrt{\left(1 + 7.94 \cdot \frac{f_{rp}}{f'_{co}}\right)} - 2 \cdot \frac{f_{rp}}{f'_{co}} \right) \right) \quad (1)$$

where f'_{cc} is the compressive strength of confined concrete, f_{rp} is the confinement pressure and f'_{co} is the unconfined strength of concrete. The compressive strain in concrete ε_{co} can be determined using the information provided by Eurocode 2 (CEN, 2004) as follows:

$$\varepsilon_{co} = \begin{cases} 0.7 \cdot f_{cm}^{0.31} \rightarrow (0.7 \cdot f_{cm}^{0.31}) < 0.0028 \\ 0.0028 \rightarrow (0.7 \cdot f_{cm}^{0.31}) \geq 0.0028 \end{cases} \quad (2)$$

where f_{cm} is the mean value of the concrete cylinder compression strength. An empirical confinement pressure formula is provided as below using experimental findings by Hu et al. (2003):

$$f_{rp} = 0.3111 \cdot \left(\frac{D}{t} - 2\right)^{-1.027} \cdot f_y \quad (3)$$

where f_y is the yield strength of the steel tube, t is the thickness of the steel tube and D is the outer diameter of the tube. Based on the study of Xu et al. (2010), the ultimate residual compressive stress, f'_{cu}, can be calculated as follows:

$$f'_{cu} = \begin{cases} f'_{cc} \cdot \left(\frac{0.1 \cdot f_y}{f'_{co}}\right)^{0.1} \rightarrow \frac{D}{t} \leq 40 \\ f'_{cc} \cdot \left(\frac{0.1 \cdot f_y}{f'_{co}}\right)^{0.1} \cdot \left(\alpha + 1(1-\alpha) \cdot e^{\left(-\frac{D}{40.t}-1\right)}\right) \rightarrow \frac{D}{t} > 40 \end{cases} \quad (4)$$

where α is an empirical parameter. Based on the paper of Hu et al. (2005), the ultimate residual compressive strain ε_{cu} can be defined as follows:

$$\varepsilon_{cu} = 11 \cdot \varepsilon_{cc} \quad (5)$$

where ε_{cc} is the compressive strain in the confined concrete. The tensile strength f'_t of concrete can be expressed using the equation below:

$$f'_t = 0.56 \cdot (f'_{co})^{0.5} \quad (6)$$

Based on the study of Kupfer et al. (1969), the biaxial compressive strength f_{ccb} can be estimated as below:

$$f_{ccb} = 1.16 \cdot f'_{cc} \quad (7)$$

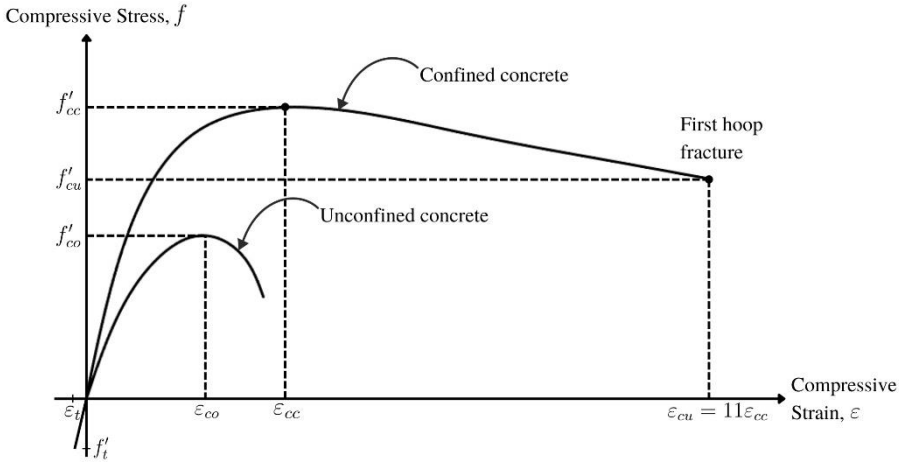

Fig. 1. Mander's stress-strain relation (1988) for both confined and unconfined concrete.

In this study, the uniaxial compressive strength, the biaxial compressive strength, and the uniaxial tensile strength values of Drucker-Prager and isotropic parameters of confined concrete were calculated using the above methodology and experimental data provided by Huang et al. (2002). Table 1 shows the concrete data utilised in the validation and parametric study, and these values are introduced to ANSYS for all models to perform nonlinear finite element simulation.

2.2. Design of the auxetic steel tubes and composite columns

When designing auxetic tubular structures, the form of the perforation is crucial since it affects the mechanical behaviour of the structure. Therefore Wang et al. (2020) presented a novel auxetic structure to minimise excessive stress concentration and provide improved auxetic behaviour. Peanut-shaped unit cells are employed to generate auxetic tubular structures and the geometric parameters of unit cells are shown in Fig. 2. Here, the small circle radius, the large circle radius, unit cell side length, distance between small circles and wall thickness of unit cell are represented as R_s, R_L, L, d and t, respectively.

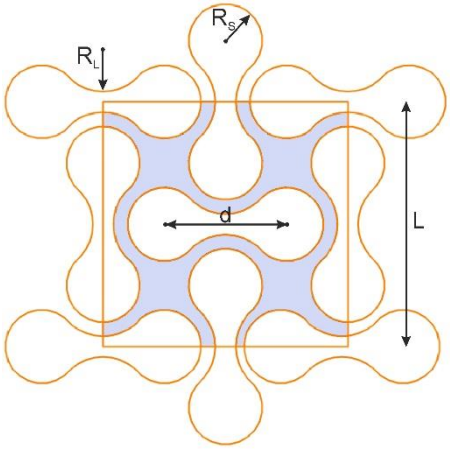

Fig. 2. Geometrical configuration of auxetic unit cell.

Table 1. Material properties of confined concrete.

Drucker-Prager plasticity parameters			Isotropic material parameters			
f'_{cc} (MPa)	f'_t (MPa)	f_{ccb} (MPa)	Unconfined compressive strength (MPa)	Modulus of elasticity (MPa)	Poisson's ratio	Density (kg/m^3)
33.68	2.92	39.07	27.15	24668	0.2	2400

Within the scope of this study, a total of six models were considered. Three have different unit cell lengths and the same porosity, while the other three have the same unit cell length and different porosity. In naming the models, auxetic steel tubes and composite columns were denoted by the letters T and C, respectively. The geometric details of unit cells used in steel tube modelling can be seen in Table 2.

Table 2. Dimensional properties of the unit cells used in auxetic steel tubes.

Tube name	R_s (mm)	R_L (mm)	L (mm)	d (mm)	t (mm)
A1T	9	12	60	30	5
A2T	7.5	10	50	25	5
A3T	4.5	6	30	15	5
B1T	4.5	6	30	15	5
B2T	3	4	30	10	5
B3T	2.5	5	30	8	5

All CFASCs are designed with a height of 300 mm, an outer diameter of 195.98 mm and a wall thickness of 5 mm by using SolidWorks software. All types of column are filled with concrete with a diameter of 185.98 mm and following the experimental study by Huang et al. (2002), CFSCs are clamped between two support plates, as seen in Fig. 3.

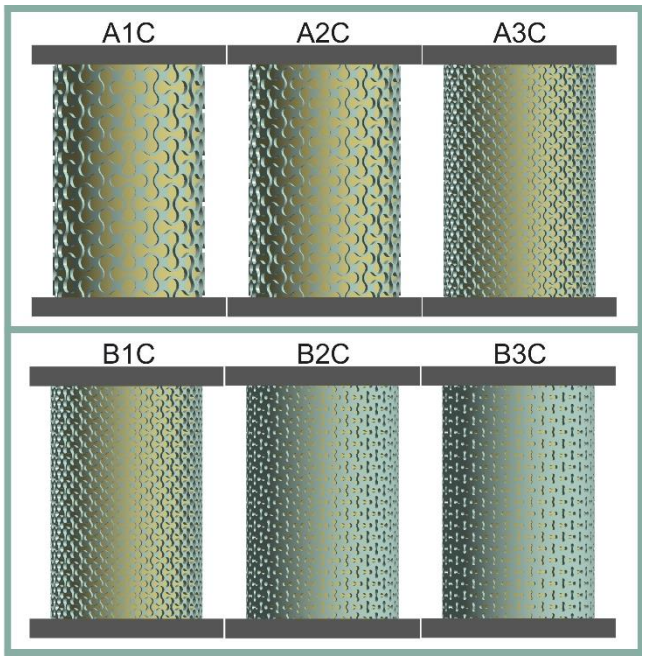

Fig. 3. Illustration of CFASC models.

The material properties of the steel tube enclosing the concrete were determined using the experimental data of the study of Huang et al. (2002), as seen in Table 3. Since the axially loaded concrete-filled steel tube was subject to high plastic deformation, isotropic hardening was also included in the analysis.

Table 3. Isotropic material properties of steel.

Yield strength (MPa)	Modulus of elasticity (GPa)	Poisson's ratio	Density (kg/m^3)
265.8	200	0.3	7850

2.3. Finite element simulation and verification

Numerical models of CFSCs were created using the Static Structural module of ANSYS 2022. In the analyses, eight-noded hexahedral elements with three translations of freedom at each node were employed for the concrete core and support plates, while four-noded tetrahedral elements were employed for all steel tubes due to the complex geometry of the auxetic steel tube. Based on several attempts to estimate an appropriate element size that provides a low computing time with relatively accurate results, the average mesh size was chosen as 10 mm for the concrete core and support plate and 2 mm for the auxetic steel tubes. The average "skewness" values of all components were also taken into account in the mesh study and kept constant between 0.2 and 0.3. Fig. 4 depicts the mesh discretisation of the finite elements used for CFASCs.

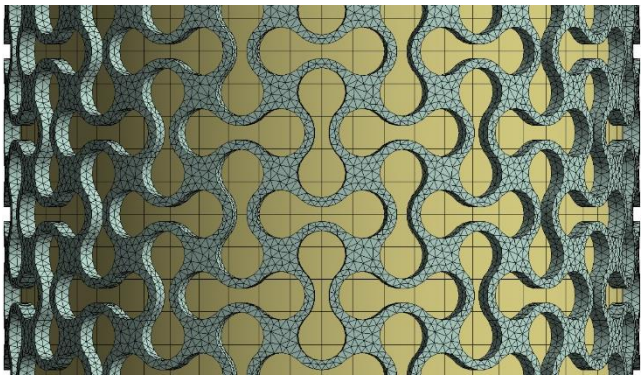

Fig. 4. Mesh discretisation of finite element model.

The interaction between concrete and steel was defined as frictional contact, and the coefficient of friction was determined as 0.6 in a direction tangent to the interaction face based on a study in the literature (Han et al. 2007). In addition, the bonded contact was employed to simulate a connection between the support plates and the steel tube. The axial load was gradually applied to the top plate, while the bottom plate was restricted for all rotations and translations. The main methodology of loading and boundary conditions is visualised in Fig. 5.

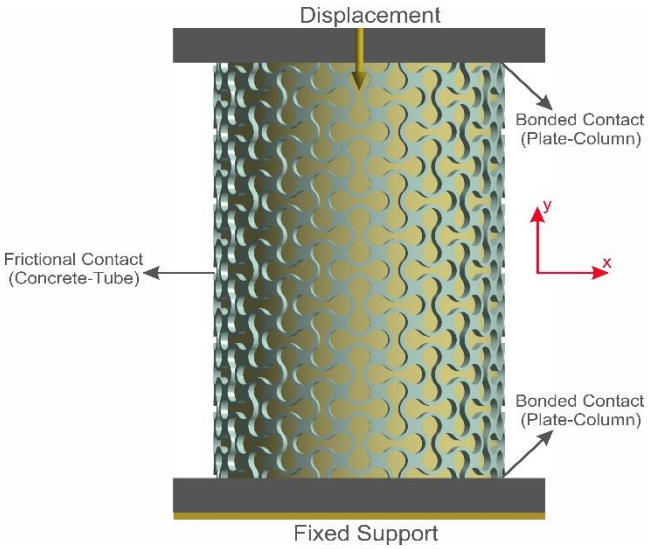

Fig. 5. Boundary and loading conditions of columns.

The mechanical characteristics of CFSC were compared with the experimental study of Huang et al. (2002) to confirm the accuracy and validity of the aforesaid numerical procedure. The CFSC used in the experiment has a height of 600 mm, an outer diameter of 200 mm and a steel tube wall thickness of 5 mm. For the finite element analysis of the validation model, the experiment's concrete and steel material properties and loading conditions were adopted by using abovementioned numerical method. At the end of the validation analysis, the load-deflection graph was produced, and ultimate compressive strength was calculated, and finally the findings were compared with the experimental results, as shown in Fig. 6. It can be seen that the load-deflection curve obtained from the finite element analysis and the curve acquired from the experiment are in agreement. While the ultimate compressive strength of the numerical analysis was 1953 kN, the ultimate compressive strength of the experiment was 2013 kN, with a relative error of 2.98%.

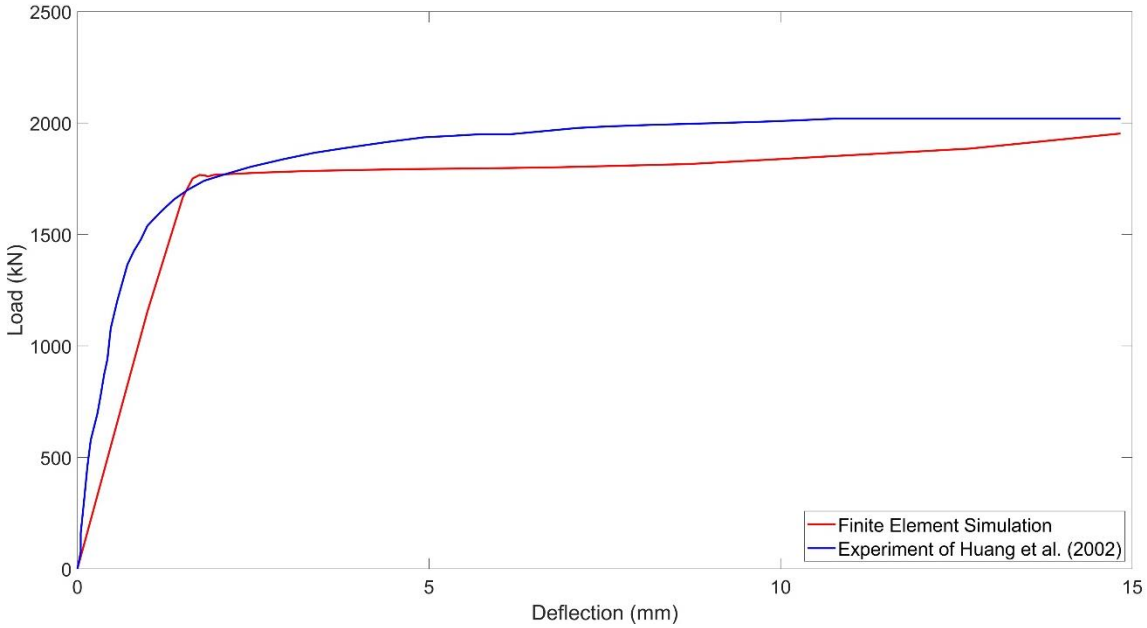

Fig. 6. Comparison of load-deflection relationships between FE simulation and experiment.

3. Results and Discussion

The ultimate load capacities of CFSCs modelled with different auxetic steel tubes were studied under axial compression. The Poisson's ratios and porosities of the auxetic tubes were determined as variable parameters and their effects on the mechanical behaviour of CFASCs were investigated. Firstly, models with different Poisson's ratios were designed without changing the porosity of the tubes to investigate only the direct effect of the Poisson's ratio on the mechanical behaviour of the columns. It was permitted to utilise different geometric parameters (R_s, R_L, L, d) to achieve the same porosity. The auxetic tubes with unit cell lengths of 30, 50 and 60 mm were created and the porosity of tubes was determined as 65.5%. Furthermore, The Poisson's ratios (ν_{xy}) were calculated using Equation 8 with the data taken from the outermost points of the centre of the models, as shown in Table 4. The A3T model, which has the largest unit cell, had the highest Poisson's ratio, while the A1T model had the lowest Poisson's ratio with the smallest unit cell. From these results, it can be seen that as the unit cell size increases, the Poisson's ratio decreases and these findings are compatible with the results of Zhang et al. (2021).

$$\nu_{xy} = -\frac{\text{lateral strain}}{\text{longitudinal strain}} = -\frac{\varepsilon_x}{\varepsilon_y} \tag{8}$$

Table 4. Poisson's ratio of auxetic steel tubes.

Tube name	L (mm)	Porosity	Poisson's ratio
A1T	60	0.655	-0.8308
A2T	50	0.655	-0.8492
A3T	30	0.655	-0.8601

Fig. 7 illustrates the load-deflection graph generated from the finite element analysis of models with identical material parameters, load-boundary conditions, and varying Poisson's ratios. The graph shows that there is a relation between the auxetic behaviour and the column's load carrying capacity. The greatest ultimate load of 1078.4 kN was achieved by the A3C model, while the lowest ultimate load of 1037.7 kN was obtained by the A1C model and the A2C model had a 1044.5 kN ultimate load. The conventional bare steel column has the same volume as the CFASC, however the bare steel column had a higher ultimate load of 1473.3 kN. As a result of their porous nature, auxetic steel tubes are inferior to bare steel.

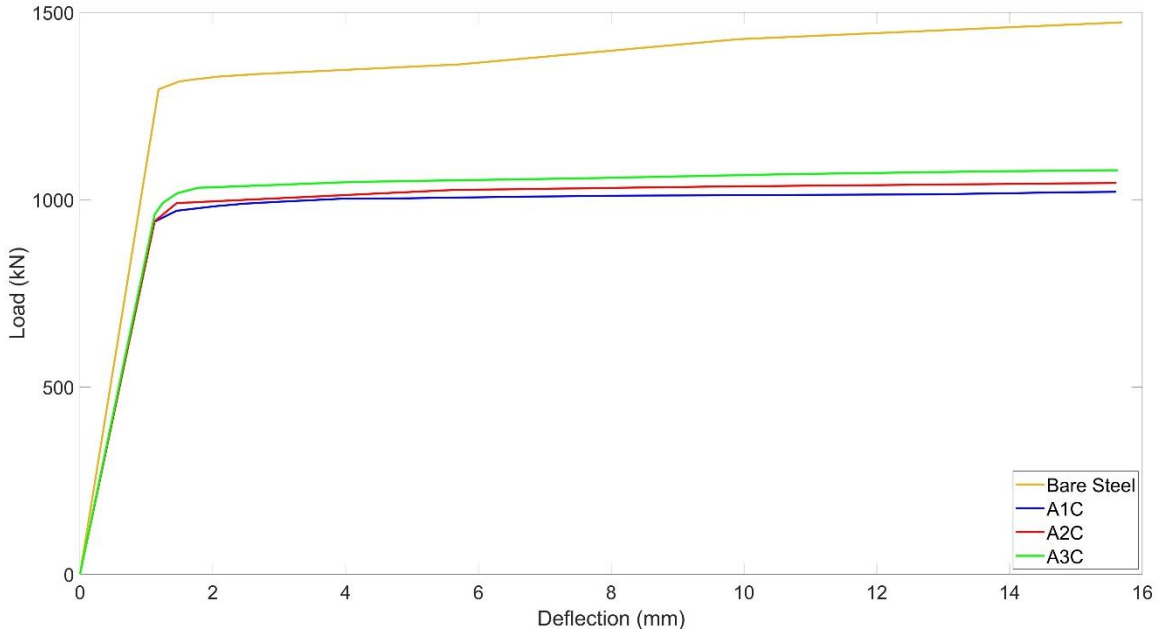

Fig. 7. Comparison of load-deflection relationships of A1C, A2C, A3C and bare steel models.

The A3C model exhibited the highest ultimate load among auxetic tubes with the same porosity, as shown in Fig. 7. Hence, further analyses were performed to thoroughly examine this structure. Therefore, the auxetic tube model with cell length L=30 mm was redesigned using different geometric parameters (R_s, R_L, d) without changing the unit cell length (L) with varied porosity, and their response to axial compression was examined. The Poisson's ratios were calculated using the approach described above. In addition, the auxetic structures' force-displacement curves were generated, and stiffness values were calculated using the slope of these curves due to changes in the porosity of the auxetic tubes. In Table 5, Poisson's ratios and stiffness values of auxetic steel tubes with different porosities are given. The highest porosity was seen in the B1T model, where the distance between the two circles was the greatest. As can be seen, as the distance (d) decreases, the space in the unit cell decreases and the structure has low porosity. Steel tubes with greater porosity exhibited more auxetic behaviour and lower stiffness values. The B3T model had the maximum stiffness value while exhibiting the least amount of auxetic behavior.

In Fig. 8, load-deflection curves of CFASC models with different tube porosity are shown. Here, although the B3C model showed the lowest auxetic behaviour, it had the highest ultimate load of 1630.7 kN. The B1C model with the highest auxetic behaviour had the lowest ultimate load of 1078.4 kN, while the B2C model had an ultimate load of 1516.9 kN. Furthermore, with increased porosity, the B3C model with a higher ultimate load than conventional bare steel was obtained. The graph shows that the influence of the Poisson's ratio on the ultimate load of models with varying porosity is nondominant. The ultimate load of the columns created by various porosities is dominated by the stiffness properties of the auxetic steel tubes. In short, whereas high porosity causes low stiffness and high auxetic behaviour, low stiffness is the primary factor in the decrease in ultimate load.

Table 5. Poisson's ratio and stiffness values of auxetic steel tubes.

Tube name	L (mm)	d (mm)	Porosity	Poisson's ratio	Stiffness (kN/mm)
B1T	30	15	0.655	-0.8601	8.6
B2T	30	10	0.293	-0.3215	427.5
B3T	30	8	0.216	-0.1021	802.2

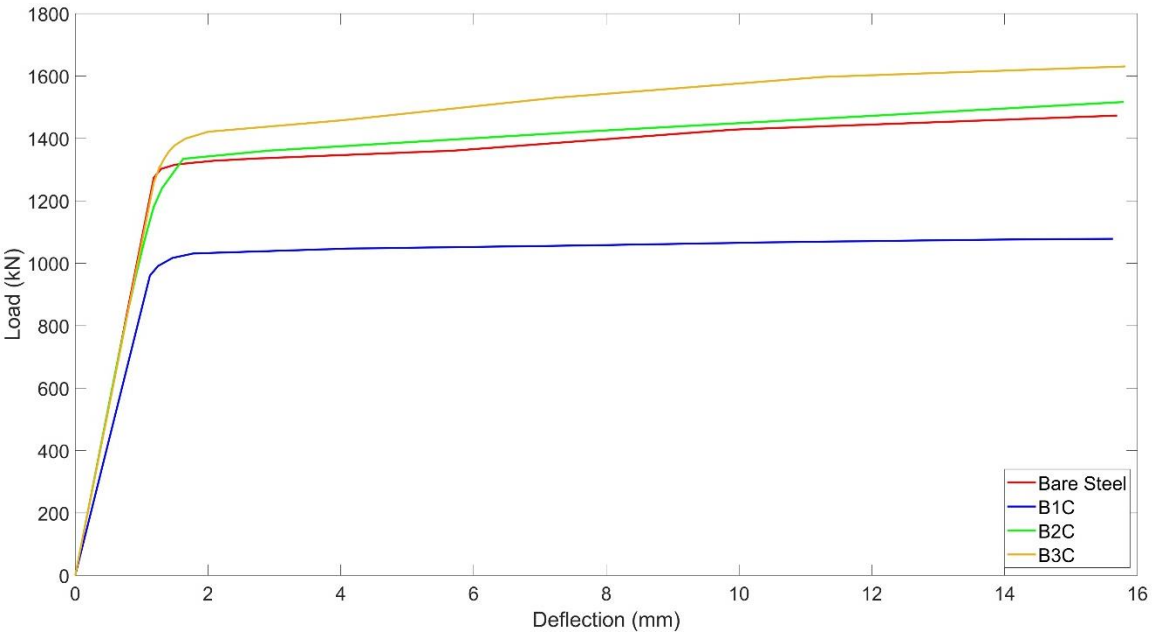

Fig. 8. Comparison of load-deflection relationships of B1C, B2C, B3C and bare steel models.

Within the scope of this research, the deformation modes and stress distributions of the structures were also studied. The maximum and average von Mises stress values of CFASCs under axial compression are given in Table 6, and the von Mises stress distributions are illustrated in Fig. 9. Since concrete has a positive Poisson's ratio, it tends to expand transversely under compression, and steel tubes with a negative Poisson's ratio counteract this to some extent. When loading was completed, the transverse expansion tendency of the concrete was dominant, causing transverse expansion in the auxetic steel tube. As a result of this expansion, high stresses were seen around the peanut perforations in all of the auxetic tubes with values between 367.34 MPa and 377 MPa. The average von Mises stresses at the concrete in all models were around 34 MPa. While the average von Mises stresses at the steel in the A1C, A2C, and A3C models were close to each other, this average stress value increased with porosity in the B1C, B2C and B3C models. Although B1C and bare steel had the same volume, the average von Mises stress of bare steel was higher.

Table 6. von Mises stresses of CFASCs.

von Mises Stress (MPa)		A1C	A2C	A3C	B1C	B2C	B3C	Bare Steel
Average	Concrete	34.2	34.3	34.4	34.4	34.4	34.6	34.9
	Steel tube	210.6	208.9	212.3	212.3	297.7	301.1	357.3
Maximum	Concrete	53.8	69.5	56.7	56.7	58.2	56.7	54.9
	Steel tube	377	368.7	367.3	367.3	376.5	376.6	377

4. Conclusions

In this study, the mechanical behaviour of concrete filled auxetic steel columns with a circular cross-section was investigated under the effect of axial compression. The finite element simulation was validated with the help of experimental results and the confirmed simulation was used to conduct a parametric study by using different geometric parameters of auxetic tubes. As a result of the parametric study, six distinct models were designed and examined, with the main parameters considering the Poisson's ratio and porosity of auxetic steel tubes. From the analyses, load-deflection curves and ultimate load capacities of all models were obtained. Moreover, the stress distributions of the concrete and the auxetic steel tubes were also thoroughly examined. A number of implications can be drawn from the findings of this study:

- The mechanical behaviour of concrete-filled auxetic steel columns can be estimated with the proposed finite element model with high accuracy and low time loss.
- Auxetic tubes with different Poisson's ratios and the same porosity have a significant effect on the ultimate load capacity of the columns as they encase the concrete core proportionally with the Poisson's ratios. Thence, steel tubes having a high auxetic tendency enhances the column's ultimate load.

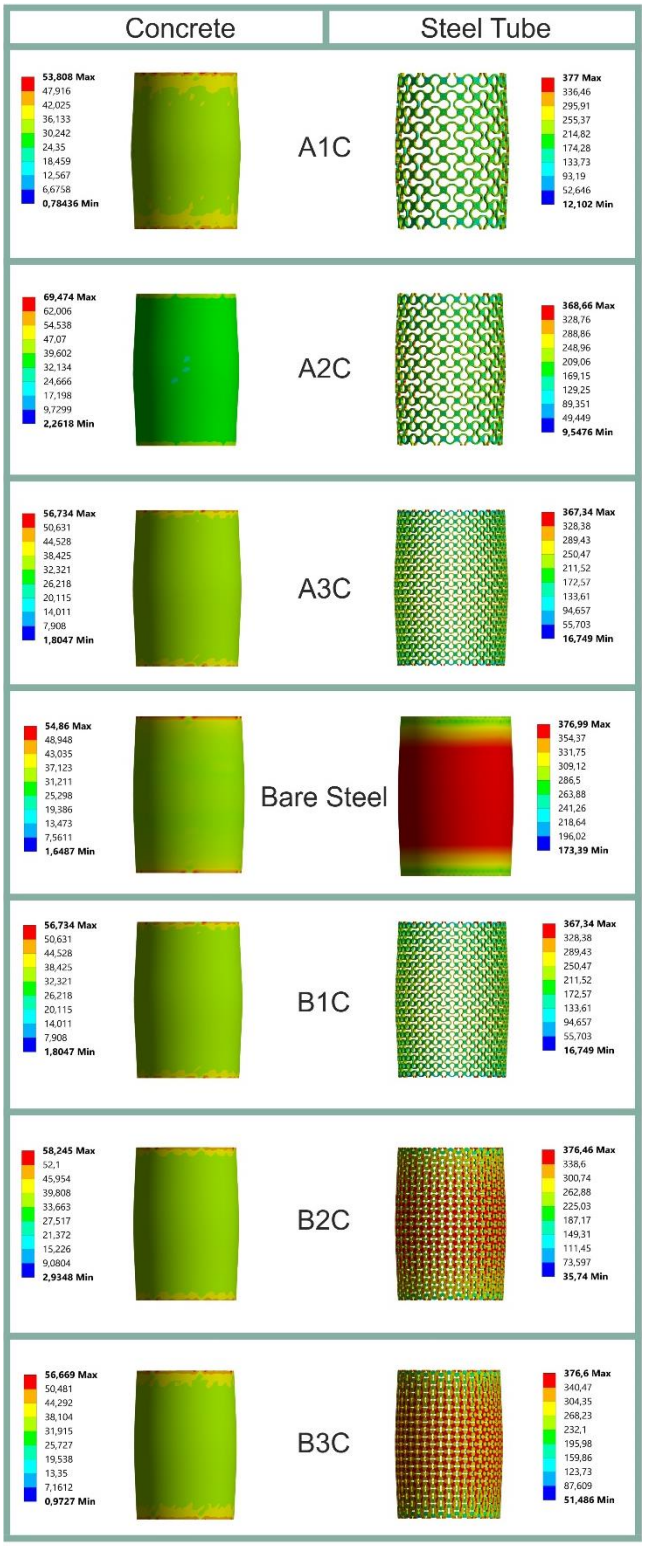

Fig. 9. Comparison of maximum von Mises stress distribution for all models.

- When porosity is considered as a variable parameter, the Poisson's ratio is no longer the determining factor, but instead stiffness is. When examining auxetic tubes with varying porosities, high porosity causes a low stiffness, which in turn decreases the ultimate load of the auxetic columns, while low porosity induces high stiffness and ultimate load.
- The ultimate loads of auxetic steel tube columns are lower than those of bare steel tube columns filled with concrete due to perforations. Nonetheless, further optimisation and parametric research can be conducted by developing new auxetic forms that yield superior outcomes to conventional concrete-filled columns.

Acknowledgements

None declared.

Funding

The authors received no financial support for the research, authorship, and/or publication of this manuscript.

Conflict of Interest

The authors declared no potential conflicts of interest with respect to the research, authorship, and/or publication of this manuscript.

References

CEN (2004). EN 1992-1-1: Eurocode 2: Design of concrete structures - Part 1-1: Buildings, rules and rules for buildings. BSI, London.

De Oliveira WLA, De Nardin S, De Cresce EALH, El Debs MK (2010). Evaluation of passive confinement in CFT columns. *Journal of Constructional Steel Research*, 66(4), 487-495.

Duarte APC, Silva BA, Silvestre N, De Brito J, Júlio E, Castro JM (2016). Finite element modelling of short steel tubes filled with rubberized concrete. *Composite Structures*, 150, 28-40.

Ellobody E, Young B (2011). Numerical simulation of concrete encased steel composite columns. *Journal of Constructional Steel Research*, 67(2), 211-222.

Gao S, Guo L, Zhang S, Peng Z (2020). Performance degradation of circular thin-walled CFST stub columns in high-latitude offshore region. *Thin-Walled Structures*, 154, 106906.

Giakoumelis G, Lam D (2004). Axial capacity of circular concrete-filled tube columns. *Journal of Constructional Steel Research*, 60(7), 1049-1068.

Gupta PK, Singh H (2014). Numerical study of confinement in short concrete filled steel tube columns. *Latin American Journal of Solids and Structures*, 11, 1445-1462.

Han LH, Yao GH, Tao Z (2007). Performance of concrete-filled thin-walled steel tubes under pure torsion. *Thin-Walled Structures*, 45(1), 24-36.

Hassanein MF, Kharoob OF, Liang QQ (2013). Behaviour of circular concrete-filled lean duplex stainless steel–carbon steel tubular short columns. *Engineering Structures*, 56, 83-94.

Hu HT, Huang CS, Wu MH, Wu YM (2003). Nonlinear analysis of axially loaded concrete-filled tube columns with confinement effect. *Journal of Structural Engineering-ASCE*, 129(10), 1322-1329.

Hu HT, Huang CS, Chen ZL (2005). Finite element analysis of CFT columns subjected to an axial compressive force and bending moment in combination. *Journal of Constructional Steel Research*, 61(12), 1692-1712.

Huang CS, Yeh YK, Liu GY, Hu HT, Tsai KC, Weng YT, Wang SH, Wu MH (2002). Axial load behavior of stiffened concrete-filled steel columns. *Journal of Structural Engineering-ASCE*, 128(9), 1222-1230.

Kedziora S, Anwaar MO (2019). Concrete-filled steel tubular (CFTS) columns subjected to eccentric compressive load. *Proceedings of the 15th Stability of Structures Symposium*, Zakopane, Poland.

Kim HG, Jeong CY, Kim DH, Kim KH (2020). Confinement effect of reinforced concrete columns with rectangular and octagon-shaped spirals. *Sustainability*, 12(19), 7981.

Kupfer H, Hilsdorf HK, Rusch H (1969). Behavior of concrete under biaxial stresses. *ACI Journal Proceedings*, 66(8), 656-666.

Lacki P, Derlatka A, Kasza P (2018). Comparison of steel-concrete composite column and steel column. *Composite Structures*, 202, 82-88.

Lacki P, Derlatka A, Kasza P, Gao S (2021). Numerical study of steel–concrete composite beam with composite dowels connectors. *Computers & Structures*, 255, 106618.

Lai MH, Ho JCM (2014). Behaviour of uni-axially loaded concrete-filled-steel-tube columns confined by external rings. *The Structural Design of Tall and Special Buildings*, 23(6), 403-426.

Liang QQ, Fragomeni S (2009). Nonlinear analysis of circular concrete-filled steel tubular short columns under axial loading. *Journal of Constructional Steel Research*, 65(12), 2186-2196.

Luo C, Ren X, Han D, Zhang XG, Zhong R, Zhang XY, Xie YM (2022). A novel concrete-filled auxetic tube composite structure: Design and compressive characteristic study. *Engineering Structures*, 268, 114759.

Ma H, Dong J, Hu G, Liu Y (2019). Axial compression performance of composite short columns composed of RAC-filled square steel tube and profile steel. *Journal of Constructional Steel Research*, 153, 416-430.

Mander JB, Priestley MJ, Park R (1988). Theoretical stress-strain model for confined concrete. *Journal of Structural Engineering*, 114(8), 1804-1826.

Munib Z, Ali MN, Ansari U, Mir M (2015). Auxetic polymeric bone stent for tubular fractures: design, fabrication and structural analysis. *Polymer-Plastics Technology and Engineering*, 54(16), 1667-1678.

Orhan SN, Erden Ş (2022a). Numerical investigation of the mechanical properties of 2D and 3D auxetic structures. *Smart Materials and Structures*, 31(6), 065011.

Orhan SN, Erden Ş (2022b). Design and finite element analysis of a novel auxetic structure. *Challenge Journal of Structural Mechanics*, 8(4), 159-165.

Ren X, Shen J, Ghaedizadeh A, Tian H, Xie YM (2016). A simple auxetic tubular structure with tunable mechanical properties. *Smart Materials and Structures*, 25(6), 065012.

Ren X, Zhang Y, Han CZ, Han D, Zhang XY, Zhang XG, Xie YM (2022). Mechanical properties of foam-filled auxetic circular tubes: Experimental and numerical study. *Thin-Walled Structures*, 170, 108584.

Schneider SP (1998). Axially loaded concrete-filled steel tubes. *Journal of Structural Engineering*, 124(10), 1125-1138.

Solak K, Orhan SN (2023). Performance evaluation of peanut-shaped tubular auxetics with enhanced stiffness: a finite element study. *Modelling and Simulation in Materials Science and Engineering*, 31(1), 015006.

Soliman KZ, Arafa AI, Elrakib TM (2013). Review of design codes of concrete encased steel short columns under axial compression. *HBRC Journal*, 9(2), 134-143.

Tao Z, Han LH (2006). Behaviour of concrete-filled double skin rectangular steel tubular beam–columns. *Journal of Constructional Steel Research*, 62(7), 631-646.

Wang H, Zhang Y, Lin W, Qin QH (2020). A novel two-dimensional mechanical metamaterial with negative Poisson's ratio. *Computational Materials Science*, 171, 109232.

Wang X, Fan F, Lai J (2022). Strength behavior of circular concrete-filled steel tube stub columns under axial compression: A review. *Construction and Building Materials*, 322, 126144.

Xu T, Xiang T, Zhao R, Zhan Y (2010). Nonlinear finite element analysis of circular concrete-filled steel tube structures. *Structural Engineering & Mechanics*, 35(3), 315.

Yu Q, Tao Z, Wu YX (2008). Experimental behaviour of high performance concrete-filled steel tubular columns. *Thin-Walled Structures*, 46(4), 362-370.

Zha X, Gong G, Liu X (2013). Study on behavior of concrete filled elliptical steel tube members part I: short and long columns under axial compression. *Advanced Steel Construction*, 9(2), 90-107.

Zhang Y, Wei Y, Bai J, Zhang Y (2019). Stress-strain model of an FRP-confined concrete filled steel tube under axial compression. *Thin-Walled Structures*, 142, 149-159.

Zhang C, Xiao SH, Qin QH, Wang H (2021). Tunable compressive properties of a novel auxetic tubular material with low stress level. *Thin-Walled Structures*, 164, 107882.

Challenge Journal of Concrete Research Letters

Research Article

Optimization of reinforced concrete frame structures and matrix displacement method

Muhammed Çoşut [a], Gebrail Bekdaş [a], Sinan Melih Nigdeli [a,*]

[a] *Department of Civil Enginering, İstanbul University-Cerrahpaşa, 34320 İstanbul, Türkiye*

ABSTRACT

In this study, reinforced concrete frame system is generated, and all structural elements which are beam and columns are optimized according to the applied distributed loads and different concrete classes by using Matlab program. Jaya algorithm which is a Metaheuristic Algorithm that enables to optimization process and finds the best cross sections, reinforcement area as well as cost of the system, is proposed. It is observed that cross-section, reinforced area as well as cost of the system are changed when concrete classes are used differently. After finding the optimum design values for frame system, the matrix displacement method is utilized to specify the system displacements and all nodes forces. Furthermore, columns and beam displacement results are not similar, and also internal forces are different for nodes. TS500 (2000) (Reinforced concrete structures design and construction rules) and TBDY (2018) (Turkey Building Earthquake Regulation) are used together to specify variables, constraints and also necessity values. The proposed method is feasible for frame structures consisting of different members.

ARTICLE INFO

Article history:
Received 28 November 2022
Revised 17 December 2022
Accepted 21 December 2022

Keywords:
Metaheuristic algorithms
Jaya algorithm
Frame system
Matrix displacement method
Optimization

1. Introduction

The pace of development in any area has been increasing significantly (Oliva et al. 2017) in recent decades (Mei and Wang 2021) in the world. Therefore, a lot of unprecedented tools, programs and systems have been invented recently such as artificial intelligence (Perea et al. 2008; Jones 2003; Sriram 2006). As recent examples, Cakiroglu et al. (2022a) exploited machine learning to estimate concrete-filled steel tubular columns' axial compression capacity. Bekdaş et al. (2022a) used harmony search to optimize the design of cylindrical walls, and they utilized ensemble learning models to forecast the best values with high accuracy. Ensemble Learning Models were also applied to civil engineering problems such as finding the rheological properties of self-compacting concrete (Cakiroglu et al. 2022b), optimization of reinforced concrete circular columns (Bekdaş et al. 2022c) and retaining walls (Bekdaş et al. 2022c). Interpretable machine learning algorithms were used to find the axial force capacity of fiber-reinforced polymer including reinforced concrete columns by Cakiroglu et al. (2022c). These developments influence our lives in terms of the quality of the system which we utilize every time. They are not limited to only one area; however, they can be in all areas, and civil engineering is at the forefront of these areas. Along with the developments, important changes are made in the features and design stages of the building systems, and it is tried to enable the use of more convenient and sustainable systems. In general, some of the main requirements requested from the building are; It should be resistant to loads that may affect it, to be aesthetic, to be applicable in terms of cost (Nigdeli and Bekdaş 2017), and the majority of the materials used should be designed without harming the environment (sustainable systems). Design engineers have to consider these while performing the design, and they use different computer programs for these circumstances. In this way, designs are made according to the loads that may affect the structure (earthquake, wind) and the purpose of use of the building, taking into account the regional soil classes. The realization of designs in this way

* *Corresponding author*. Tel.: +90-212-473-7070 ; Fax: +90-212-889-1887 ; E-mail address: melihnig@iuc.edu.tr (S. M. Nigdeli)
ISSN: 2548-0928 / DOI: https://doi.org/10.20528/cjcrl.2023.01.002

prevents deviations from the regulations, and by doing it in accordance with its purpose, in case of any possible impact (earthquake load), it prevents the systems or the structure from being significantly damaged. Nonetheless, regulations allow structures with certain safety coefficients to be damaged in a controlled manner, instead of the structure being damaged unexpectedly. Demanding this type of damage like this is to prevent loss of life.

Frame systems are used extensively in certain regions of some countries. In the case of seismicity in some regions and higher than certain story heights, it is not preferred much. Even if it is preferred, it should be supported with different building carrier elements. The most important reason for the overuse of these systems is their low cost. Since the energy dissipation that will occur in earthquake effects is less than other building systems, they are the systems that suffered the most damage or collapse under the effects of earthquakes (Doğangün 2019). As a consequence, to increase the earthquake performance, the rigidity of the structure is increased by adding shear walls to the framed systems. In this way, most of these dynamic loads are covered by shear walls in case of earthquake or wind effects. Ulusoy et al. (2020) studied to find the optimal design of reinforced concrete beams by examining the strength of concrete, and they used Metaheuristic Algorithm in this process. Leps and Sejnoha (2003) utilized simulated annealing, which is a metaheuristic algorithm, to optimize the continuous beam. In order to reach the optimum cost for reinforced concrete slabs, Shayegan (2022) used various metaheuristic algorithms and hybrid algorithms, and Ghandi et al. (2017) utilized cuckoo search algorithm.

In this study, the cross-section designs of the elements of the frame system are carried out using metaheuristic algorithms which have been utilizing engineering problems to reach optimum value, and optimum section designs are carried out in accordance with the regulations such as TS500 (2000) and TBDY (2018). Before the sections are determined by optimization, some material properties and constraint conditions and the maximum-minimum values of the variables which are taken by Balling and Rao (1997) are added to the algorithms. As a result of these, the forces (shear and axial forces) formed in all joint areas and the resulting displacement values are found and compared using the Matrix Displacement Method according to the optimum cross-section dimensions.

2. Methodology

2.1. Design of reinforced concrete frame structures

Reinforced concrete frame structure which consists of columns and beams has to be designed by using regulations. These regulations include some design values, constraints as well as limitation length of column and beam size. All features are used in the optimization process to reach optimum size by Mayencourt and Mueller (2020) and cost design.

Beam and column have various features to calculate the appropriate design. Some formulas show below for beam calculations. Eq. (1) demonstrates the decreasing amount of materials values to stay safe design. Beams have 2 sides which are the compression region as well as tensile region, and these effects should same to balance themselves Eq. (2). In addition, Eq. (3) shows stress block depth. Fig. 1 shows the beam section.

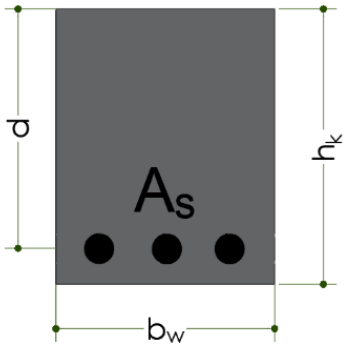

Fig. 1. Beam cross-section.

Regarding the given equations which are related to beam and column design, a is the stress block depth, M is the moment that has an impact on the structure, d is the distance from center of longitudinal tensile reinforcement from over tightening, f_{yd} is the design yield strength for steel, f_{cd} is the compressive strength of concrete design, f_{ck} is the concrete's characteristic compressive strength, f_{ctk} is the characteristic axial tensile strength of concrete, ρ_b is the balanced reinforcement ratio, and $k1$ changes according to the concrete class.

$$f_{cd} = \frac{f_{ck}}{1.5} \text{ and } f_{yd} = \frac{f_{yk}}{1.15} \quad (1)$$

$$F_c = F_s = 0.85 \times f_{cd} \times b_w \times a \quad (2)$$

$$a = d - \sqrt{d^2 - \frac{2 \times M}{0.85 \times f_{cd} \times b_w}} \quad (3)$$

For Eq. (4), after finding the reinforcement area, it is compared whether it is between the maximum and minimum reinforcement ratio.

$$0.8 \times \frac{f_{ctd}}{f_{yd}} \leq \rho = \frac{A_s}{b_w \times d} = \frac{\frac{M}{f_{yd} \times \left(d - \frac{a}{2}\right)}}{b_w \times d} \leq \begin{cases} 0.85 \times \rho_b \\ 0.02 \\ 0.235 \times \frac{f_{cd}}{f_{yd}} \end{cases} \quad (4)$$

Some formulas show below for column calculations. A reinforced concrete column has to provide adequate capacity to withstand axial force and bending moment (Camp and Hug 2013). Fig. 2 shows the column section. In order to find column cross-sections, it is necessary to use some of the equations. With Eq. (5), neutral axis distance is determined for balanced conditions, while Eqs. (6) and (7) are used for finding stress block depth and for finding axial pressure force respectively. d' is known as concrete cover.

$$c_b = \frac{600}{600+f_{yd}} d \quad (5)$$

$$a_b = k_1 \times c_b \quad (6)$$

$$N_b = 0.85 \times f_{cd} \times a_b \times b \quad (7)$$

After finding the axial pressure force, it is compared with Eqs. (8) and (9), and therefore, it is checked whether rebar is needed or not. While stress block depth can be found by Eq. (10), reinforcement area for the column can easily be found by Eq. (11).

$$\psi_c = 0.85 \times \frac{d'}{h} \times \frac{600}{600-f_{yd}} \quad (8)$$

$$\text{Control} = \frac{N_d}{b \times h \times f_{cd}} \quad (9)$$

$$a = \frac{N_d}{0.85 \times b \times f_{cd}} \quad (10)$$

$$A_{st} = 2 \times \frac{M - N_d \times (\frac{h}{2} - \frac{a}{2})}{f_{yd} \times (d - d')} \quad (11)$$

2.2. Matrix displacement method

There are many displacement methods and one of them is the matrix displacement method, which is the method that generates the unknowns of the displacement components of the system. The matrix displacement method is the determination of the displacement value of the structure under the static and dynamic loads that may be effective on the structure, the internal force values and the deformation effects that may occur. Impact such as loads, displacements and reaction force in the system are defined in the global coordinate system. Despite this, the section effects are formed by changing relative to the global coordinate system according to the location of the building element and it is called the local coordinate system. Transitions from the global coordinate system to the local coordinate system (Fig. 3) or completely reversible can be done easily with angles.

Some of the names of the angles in formulations are abbreviated. It can be easily comprehended to how they can use it.

For abbreviation: $S = \sin(\theta)$, $C = \cos(\theta)$

$$X_L = Y_G \times \sin(\theta) + X_G \times \cos(\theta) \longrightarrow X_L = Y_G \times S + X_G \times C \quad (12)$$

$$Y_L = Y_G \times \cos(\theta) - X_G \times \sin(\theta) \longrightarrow Y_L = Y_G \times C - X_G \times S \quad (13)$$

Although the global coordinate's axis names are X_G and Y_G, the Local coordinate's axis names are X_L and Y_L. Thus, these can easily be seen in Equations. Eqs. (12) and (13) are used to reach Local coordinate locations and these abbreviations can be seen respectively. A matrix which is given as Eq. (14) enables finding Local Coordinate property. The stiffness matrices in local and global coordinates have the relation given in Eq. (15). Node displacement (Kaveh and Zaerreza 2022) can be found in Eq. (16), while internal loads can be found in Eq. (17).

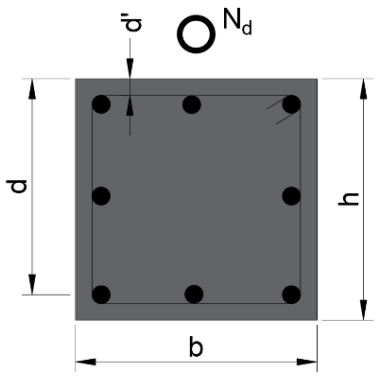

Fig. 2. Column cross-section.

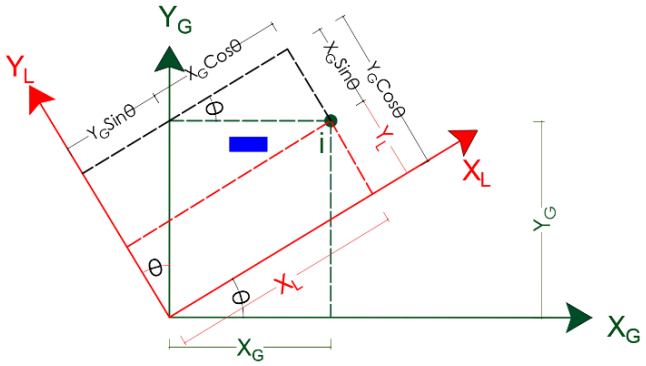

Fig. 3. Global-local coordinate system.

$$\begin{bmatrix} X_{Li} \\ Y_{Li} \\ \theta_{Li} \\ X_{Li} \\ Y_{Li} \\ \theta_{Li} \end{bmatrix} = \begin{bmatrix} C & S & 0 & 0 & 0 & 0 \\ -S & C & 0 & 0 & 0 & 0 \\ 0 & 0 & 1 & 0 & 0 & 0 \\ 0 & 0 & 0 & C & S & 0 \\ 0 & 0 & 0 & -S & C & 0 \\ 0 & 0 & 0 & 0 & 0 & 1 \end{bmatrix} \cdot \begin{bmatrix} X_{Gi} \\ Y_{Gi} \\ \theta_{Gi} \\ X_{Gi} \\ Y_{Gi} \\ \theta_{Gi} \end{bmatrix} \quad (14)$$

$$[K_G] = [R]^T * [K_L] * [R] \quad (15)$$

$$[\Delta_L]_F = [R]_F * [\Delta_G]_F \quad (16)$$

$$[P_L]_F = [K_L]_F * [\Delta_L]_F \quad (17)$$

P refers to internal force, K refers to stiffness matrix and Δ refers to displacement. Moreover, some features of materials and cross-section values are necessary to know in order to find stiffness matrix results. As seen in Eq. (18), these features are seen as E, A, I as well as L on the matrix. E is the modulus of elasticity, A is the area of cross-section, I is the moment of inertia as well as L is the length of structure elements.

$$[K_L]_F = \begin{bmatrix} \frac{EA}{L} & 0 & 0 & -\frac{EA}{L} & 0 & 0 \\ 0 & \frac{12EI}{L^3} & \frac{6EI}{L^2} & 0 & -\frac{12EI}{L^3} & \frac{6EI}{L^2} \\ 0 & \frac{6EI}{L^2} & \frac{4EI}{L} & 0 & -\frac{6EI}{L^2} & \frac{2EI}{L} \\ -\frac{EA}{L} & 0 & 0 & \frac{EA}{L} & 0 & 0 \\ 0 & -\frac{12EI}{L^3} & -\frac{6EI}{L^2} & 0 & \frac{12EI}{L^3} & -\frac{6EI}{L^2} \\ 0 & \frac{6EI}{L^2} & \frac{2EI}{L} & 0 & -\frac{6EI}{L^2} & \frac{4EI}{L} \end{bmatrix} \quad (18)$$

2.3. Jaya algorithm

Metaheuristic algorithms include Particle Swarm Optimization (PSO) developed by Kennedy and Eberhart (2001), Jaya Algorithm developed by Rao (2016), the Teaching Learning Based Optimization (TLBO) developed by Rao (2012). Design time, cost and sufficient design (Giran et al. 2017) can be also designed by algorithms. Jaya algorithm is working more efficiently in various problems to reach objective functions in a short time. To exemplify for one of the column problems, Cakiroglu and Bekdaş (2022) carried out the maximum axial load for a concrete filled steel tubular column by using Jaya algorithm which is 10759 kN. Jaya algorithm process is generally similar just some formulations can be changed according to problems. After generating the initial matrix, solutions are compared according to the Jaya algorithm's generated new solutions and initial matrix solutions to choose the best one in order to reach the minimum objective function. Eq. (19) is the Jaya algorithm equation that is used in the optimization process.

$$X'_{i,\text{new}} = X_{i,j} + r()\left(X_{i,g_{\text{best}}} - |X_{i,j}|\right) - r()\left(X_{i,g_{\text{worst}}} - |X_{i,j}|\right) \quad (19)$$

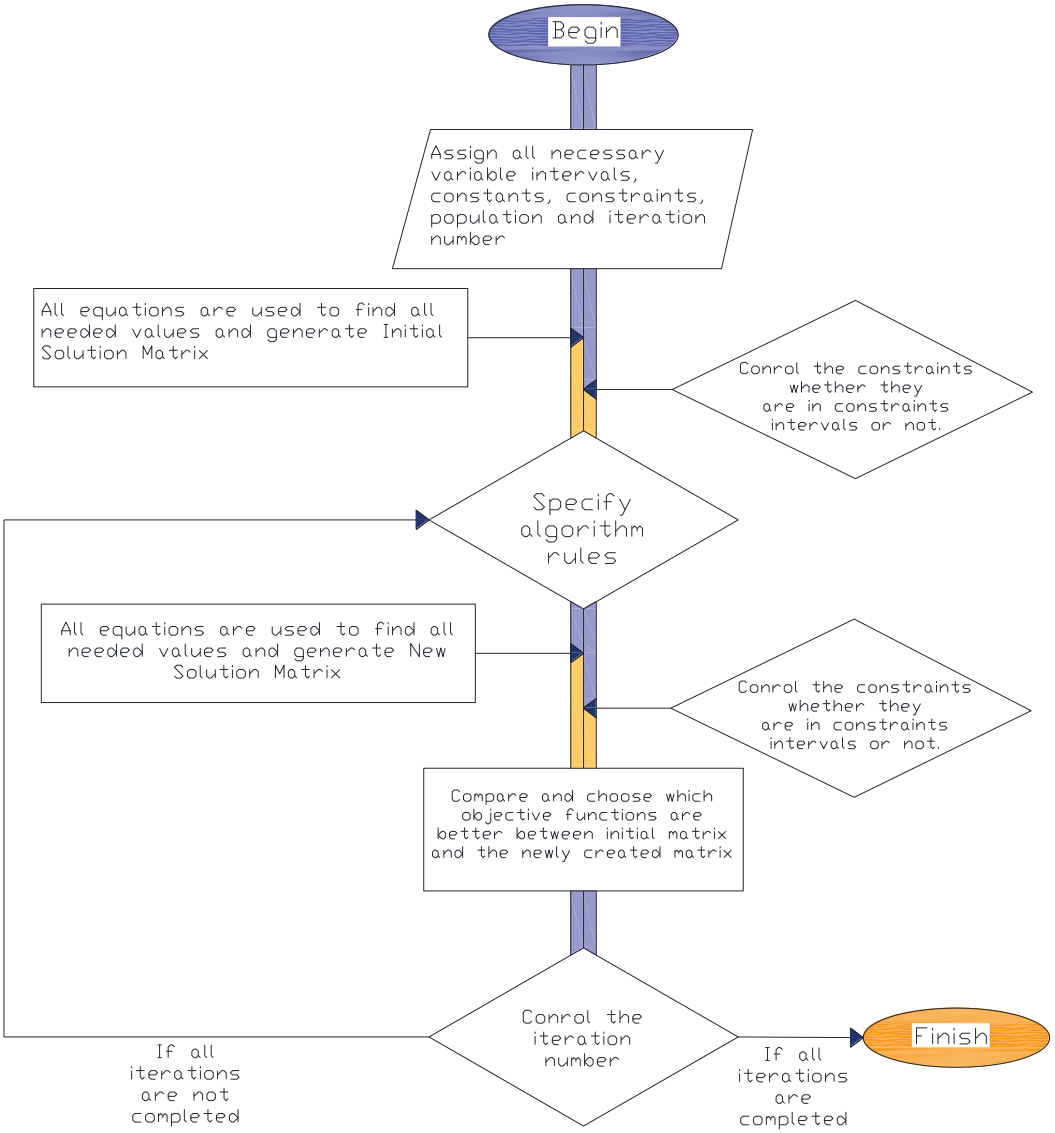

Fig. 4. Optimization process using Jaya algorithm.

Fig. 4 delineates the flowchart which is related Jaya algorithm. There are several steps to reach objective function, and they consist of preparing optimization, solving equations as well as comparing matrices to find the best values for problems. Iteration steps continue until the iteration number completes exactly its maximum values.

3. Numerical Example

Fig. 5 demonstrates the frame system which is optimally designed via the Jaya algorithm.

Table 1 consists of variables, constants and cost values. The clear cover is chosen as 30 mm.

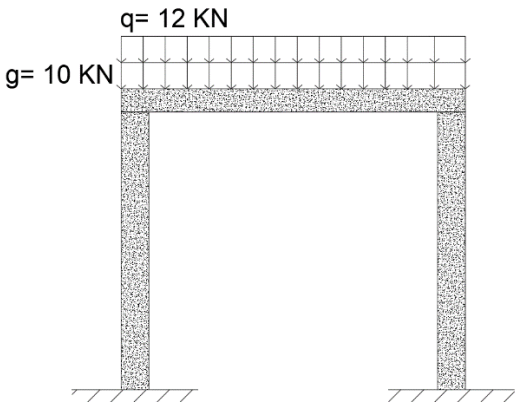

Fig. 5. Frame structure.

The given frame structure is solved by Jaya Algorithm in order to reach the most design cost. To complete this process, the algorithm and necessary equations are added to Matlab program. The objective function is specified as Eq. (20).

$$\text{FrameSystemCost} = \text{TotalConcreteVolume} \times C_c + \text{TotalSteelArea} \times C_s + \text{TotalArea} \times (C_{k,m}+C_{k,i}) \quad (20)$$

Table 2 has different constraints for the design of the frame system which consist of a beam and two columns. These constraints are about comparing maximum and minimum reinforced area, checking stress block depth and also comparing axial force.

Table 1. Design values.

Explanation	Symbol	Unit	Value
Beam min-max section width	$b_{w,\text{min-max}}$	mm	250-400
Beam min-max section height	$h_{k,\text{min-max}}$	mm	400-600
Column min-max section width	$b_{\text{min-max}}$	mm	300-600
Column min-max section height	$h_{\text{min-max}}$	mm	300-600
Live load - Dead load	q-g	kN/m	12-10
Beam length - Column height	L-H	m	6-3
Yield strength of concrete	f_{yk}	MPa	420
Specific gravity of steel	γ_s	t/m³	7.86
Cost of concrete per unit volume	C_c	TL/m³	C25/30 - 790 C30/37 - 820 C35/45- 875
Cost of steel per unit weight	C_s	TL/ton	14900
Cost of formwork material - Labour	$C_{k,m}$ -$C_{k,i}$	TL/m	104-60
Axial load	N_d	kN	300
Stirrup	Ø		8

Table 2. Constraint for the design of the frame system.

TS500	Constraints
Column	$g_1 = \psi < \frac{N_d}{b \times h \times f_{cd}}$
	$g_2 = 0.04$
	$g_3 \leq \begin{cases} b/3 \\ 100\ mm \end{cases}$
Beam	$g_4 = 0 < d - \sqrt{a} < h_k$
	$g_5 = \text{beam reinforcement area} < \begin{cases} 0.85 \times \rho \\ 0.02 \\ 0.235 \times \frac{f_{cd}}{f_{yd}} \end{cases}$
	$g_6 = \text{beam reinforcement area} \geq 0.8 \times \frac{f_{ctd}}{f_{yd}}$

In this problem, the Jaya algorithm is used as Metaheuristic Algorithm to find cost and cross sections. The result of this system is shown in Table 3 and the maximum cost occurs by using C25/30. Although concrete cost is the lowest compared to others, the necessity reinforced area (A_s) is the biggest one. That's why the cost of using C25/30 is more expensive.

Fig. 6 shows the positive direction notation and num-

bering of the frame structure. Positive direction property is used, when these notations show. With the Matrix displacement method, these notations are used in the algorithm to reach internal forces as well as displacement.

Table 3. Results of optimization.

Explanation	Beam			Column			Cost
	b (mm)	h (mm)	A_s (mm^2)	b (mm)	h (mm)	A_s (mm^2)	F(x)(TL)
C25/30	250	400.0	834.0	327.17	342.75	1214.5	3290.0
C30/37	250	400.0	814.0	300.00	350.70	1052.0	3232.0
C35/45	250	404.6	789.3	300.00	348.20	1044.5	3284.6

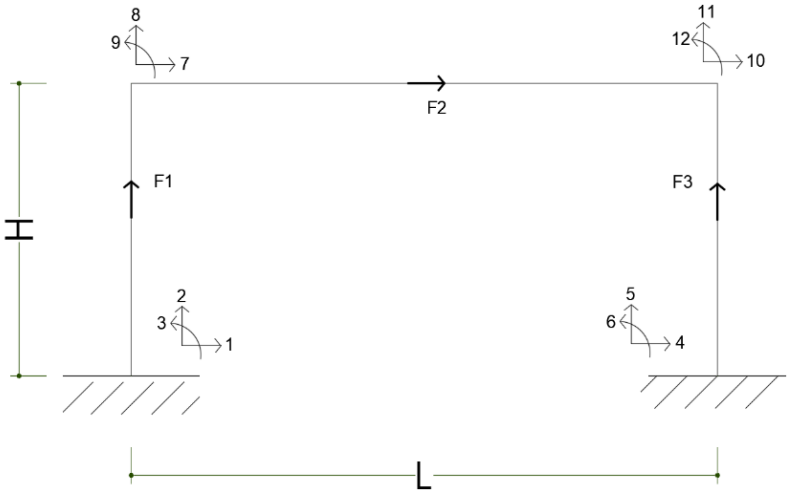

Fig. 6. Frame structure with numbering and direction rotation.

The process of the Matrix displacement method has different steps. It should be followed as below orders.

- The global axis stiffness matrix is translated to the local axis for each element.
- Transformation matrix is created for each element.
- Global axis stiffness matrix is found for each element
- The stiffness matrix of the system is found by superposing the global axis stiffness matrices for all elements.
- Displacement calculations are completed for each point by using loads affecting the system.
- The internal forces of each point are found according to the displacement values found.

Table 4 includes F1's data as internal force and displacement while Table 5 includes F3's data as internal force and displacement and also Table 6 includes F2's data as internal force and displacement. There are 12 nodes that have different features because of their locations. Looking at the tables in more detail, there is no displacement in 1-2-3 nodes and 1-7 nodes are the same amount of force with different directions. Table 3 consists of beam responses. All nodes have displacement because of non-fixed features.

Table 4. Internal forces and displacement for F1.

Explanation	1 (kN)	2 (kN)	3 (kNm)	7 (kN)	8 (kN)	9 (kNm)
$[P_L]_{F1}$ (Internal Force)	-99.60	33.19	33.04	99.6	-33.19	66.53
$[\Delta_L]_{F1}$ (Displacement)	0	0	0	$1.66*10^{-4}$	$4.98*10^{-5}$	0.0037

Table 5. Internal forces and displacement for F2.

Explanation	4 (kN)	5 (kN)	6 (kNm)	10 (kN)	11 (kN)	12 (kNm)
$[P_L]_{F2}$ (Internal Force)	-99.60	-33.19	-33.04	99.6	33.19	-66.53
$[\Delta_L]_{F2}$ (Displacement)	0	0	0	$1.66*10^{-4}$	$-4.98*10^{-5}$	-0.0037

Table 6. Internal forces and displacement for F3.

Explanation	7 (kN)	8 (kN)	9 (kNm)	10 (kN)	11 (kN)	12 (kNm)
$[P_L]_{F3}$ (Internal Force)	-33.19	$2.6 * 10^{-15}$	33.07	33.19	$-2.6*10^{-15}$	-33.07
$[\Delta_L]_{F3}$ (Displacement)	$-4.98 * 10^{-5}$	$1.7 * 10^{-4}$	0.0037	$4.98*10^{-5}$	$1.66*10^{-4}$	-0.0037

It is shown in Tables 4-6 by finding displacements and internal force values for each bar. From these tables, the displacements for the fixed numberings (1 2 3 4 5 6) for the frame systems are found to be zero, while the displacements will occur at the non-fixed (7 8 9 10 11 12) nodes and these displacements will take the same values in two opposite points.

4. Conclusions

In the case of using different concrete classes, reinforced area calculations were made in such a way that the values of the cross-section dimensions of the frame system elements and the boundary conditions were provided, and cost optimization was made for each concrete class, and the objective function was achieved, which all optimization steps are generated on Matlab. It is seen that the beam cross-section values for each concrete class are 250 mm and nearly 400 mm, while the column cross-section values take values in the range of 300-350 mm. Concrete classes have different cost values while the price of reinforcement is taken as the same price on a per-ton basis. In other words, the cost of the reinforcement varies depending on the area of reinforcement that is required to be used in the system. From this, it has been calculated that the design with concrete class C25/30 is more expensive than other concrete class designs, but there is not much change in the section dimensions. There is a cost difference of approximately 1.75% between the C25/30 and C30/40 concrete class design costs. While between the C25/30 and C35/45 concrete class design costs difference is roughly 0.16%. Moreover, after all these processes such as finding the optimum cross-section area, the necessary features are utilized to reach the system of internal forces and all nodes displacements. By using the Matrix displacement method, the system is divided into 3 parts which are F1, F2, as well as F3 and these are calculated separately. Non-fixed points can displace according to loading. The internal load can easily be seen that all separated parts same values in the same direction.

Acknowledgements

None declared.

Funding

The authors received no financial support for the research, authorship, and/or publication of this manuscript.

Conflict of Interest

The authors declared no potential conflicts of interest with respect to the research, authorship, and/or publication of this manuscript.

References

Balling R, Yao X (1997). Optimization of Reinforced Concrete Frames. *J. Struct. Eng.,* 123, 193-202.

Bekdaş G, Cakiroglu C, Islam K, Kim S, Geem ZW (2022a). Optimum design of cylindrical walls using ensemble learning methods. *Applied Sciences,* 12, 2165.

Bekdaş G, Cakiroglu C, Kim S, Geem ZW (2022b). Optimization and predictive modeling of reinforced concrete circular columns. *Materials*, 15(19), 6624.

Bekdaş G, Cakiroglu C, Kim S, Geem ZW (2022c). Optimal dimensioning of retaining walls using explainable ensemble learning algorithms. *Materials*, 15(14), 4993.

Cakiroglu C, Bekdaş G (2022). Optimization of axial load carrying capacity of CFST stub columns. *Challenge Journal of Concrete Research Letters*, 13(1), 1-4.

Cakiroglu C, Islam K, Bekdaş G, Isikdag U, Mangalathu S (2022a). Explainable machine learning models for predicting the axial compression capacity of concrete filled steel tubular columns. *Construction and Building Materials*, 356, 129227.

Cakiroglu C, Bekdaş G, Kim S, Geem ZW (2022b). Explainable ensemble learning models for the rheological properties of self-compacting concrete. *Sustainability*, 14(21), 14640.

Cakiroglu C, Islam K, Bekdaş G, Kim S, Geem ZW (2022c). Interpretable machine learning algorithms to predict the axial capacity of FRP-reinforced concrete columns. *Materials*, 15(8), 2742.

Camp CV, Huq F (2013). CO2 and cost optimization of reinforced concrete frames using a big bang-big crunch algorithm. *Engineering Structures*, 48, 363-372.

Doğangün A (2019). Betonarme Yapıların Hesap ve Tasarımı. Birsen Yayınevi, İstanbul, Türkiye.

Ghandi E, Shokrollahi N, Nasrolahi M (2017). Optimum cost design of reinforced concrete slabs using cuckoo search optimization algorithm. *International Journal of Optimization in Civil Engineering*, 7(4), 539-564.

Giran Ö, Temur R, Bekdaş G (2017). Resource constrained project scheduling by harmony search algorithm. *KSCE Journal of Civil Engineering*, 21(2), 479-487.

Jones MT (2003). Artificial intelligence application programming. Charles River Media, Hingham (Massachusetts), USA.

Kaveh A, Zaerreza A (2022). Comparison of the graph- theoretical force method and displacement method for optimal design of frame structures. *Structures,* 43, 1145-1159.

Kennedy J, Eberhart RC, Shi Y (2001). Swarm Intelligence. Morgan Kaufmann Publishers, London, England.

Leps M, Sejnoha M (2003). New approach to optimization of reinforced concrete beams. *Computers and Structures*, 81, 1957-1966.

Mayencourt P, Mueller C (2020). Hybrid analytical and computational optimization methodology for structural shaping: Material-efficient mass timber beams. *Engineering Structures*, 215, 110532.

Mei L, Wang Q (2021). Structural optimization in civil engineering: a literature review. *Buildings*, 11(2), 66.

Niğdeli SM, Bekdaş G (2017). Optimum design of RC continuous beams considering unfavourable live-load distributions. *KSCE Journal of Civil Engineering,* 21(4), 1410-1416.

Olivia M, Barone G, Navarra G (2017). Optimal design of nonlinear energy sinks for SDOF structures subjected to white noise base excitations. 145, 135-152.

Perea C, Alcala J, Yepes V, Vidosa FG, Hospitaler A (2008). Design of reinforced concrete bridge frames by heuristic optimization. *Advances in Engineering Software*, 39, 676-688.

Rao RV (2011). Teaching-Learning based optimization: A novel method for constrained mechanical design optimization problems. *Computer Aided Design*, 43, 303-315.

Rao RV (2016). Jaya: A simple and new optimization algorithm for solving constrained and unconstrained optimization problems. *International Journal of Industrial Engineering Computations,* 7, 19-34.

Shayegan DS (2022). Optimum cost design of reinforced concrete slabs using a metaheuristic algorithm. *International Journal of Optimization in Civil Engineering*, 12(4), 545-555.

Sriram RD (2006). Artificial intelligence in engineering: personal reflections. *Advanced Engineering Informatics,* 20, 3–5.

TBDY (2018). Türkiye Bina Deprem Yönetmeliği. Afet ve Acil Durum Yönetimi Başkanlığı, Ankara, Türkiye.

TS 500 (2000). Betonarme Yapıların Tasarım ve Yapım Kuralları (Requirements for Design and Construction of Reinforced Concrete Structures). Türk Standardları Enstitüsü, Ankara, Türkiye.

Ulusoy S, Kayabekir AE, Bekdaş G, Nigdeli SM (2020). Metaheuristic algorithms in optimum design of reinforced concrete beam by investigating strength of concrete. *Challenge Journal of Concrete Research Letters*, 11(2), 26-30.

Challenge Journal of Concrete Research Letters

Case Study

Cause of distress of an old building through analytical and micro–analytical methods – a case study

Rajappan Preetha [a,*], Kalpana Kumari [a], Balakrishnan Sakthi [a], Chandrasekharan Nair Harikumar [a], Haneef Ibrahim Abdul Gani [a]

[a] *Indira Gandhi Centre for Atomic Research, 603102 Kalpakkam, Tamilnadu, India*

ABSTRACT

The case study pertains to the methods such as nondestructive, semi-destructive, chemical, electrochemical and micro-analytical, utilized to assess the cause of cracking and spallation of a reinforced concrete building near to the eastern coastline of India. Cause of degradation of the structure is assessed to arrive at the appropriate repair methodology. From the analysis methods, direct cause of failure could not be attributed to a single cause since many factors co-exist such as structural cracking, carbonation and presence of chloride and the synergistic effect; hence concludes that an appropriate repair methodology has to be evolved to address each issue.

ARTICLE INFO

Article history:
Received 7 September 2022
Revised 27 October 2022
Accepted 4 November 2022

Keywords:
Concrete
Corrosion
Reinforcement
Chloride
Carbonation

1. Introduction

Technical service life of a reinforced concrete building is the time in service at the end of which structural safety is unacceptable due to either material degradation or exceedance of the load carrying capacity or both, in which case repair strategy may be adopted if it is still economically more advantageous than replacement, as mentioned in ACI 365.1R (2000). Cause of degradation of the structure is to be assessed to arrive at the appropriate repair methodology. The process of chemical and physical deterioration of concrete with time is a function of presence and transport of deleterious materials in concrete and the synergistic effect of applied loads as well explained in his review by Ahmad (2003). The rate and extent of this transport is largely dependent on concrete pore structure, presence of cracks and the microclimate of the surface of concrete. Though the coefficient of permeability of concrete is dependent on concrete materials and the method of execution, it is also influenced by age. Major reason as mentioned in Dhawan et al. (2014) for deterioration of a reinforced concrete building is the reinforcement corrosion which is usually manifested as cracking, staining and spallation. This highlights the importance of in service inspection and routine maintenance of buildings.

The case study pertains to an office building built in the 1970s.This building is within 1km of the eastern coast line of India. This is a highly corrosive belt of peninsular India as per Natesan et al. (2005). The building serves as the main design office and has always been the most utilized office space in a power plant campus. Being one of the first buildings in the campus, several novel architectural features like slender columns, waffle slab, hanging staircase and long wide windows with deep sunshades were conceived to give a perfect ambience of a well ventilated design office with natural light. The basis of analysis and design of the structure is the national standard, IS 456 (1968) of the early '70s. The structure has seen a life span of 48 years with proper maintenance. It has been observed recently that, few of the reinforced concrete columns have started cracking and spalling just above the ground level. The distress in columns started with vertical cracking in the cover region, followed by spallation. This study aims at estimating the extent and type of degradation of the building analytically and micro-analytically (Qazweeni et al.) and interpreting the results.

* *Corresponding author*. Tel.: +91-944-412-9806 ; Fax: +91-044-274-80306 ; E-mail address: predinesh@igcar.gov.in (R. Preetha)
ISSN: 2548-0928 / DOI: https://doi.org/10.20528/cjcrl.2023.01.003

2. Structural Layout of the Building

The building is a reinforced concrete (RC) framed construction with brick masonry infill. It is an H –shaped double-storied structure with parallel plan dimension of 72×13.6 m and a connecting corridor. The height of each floor is 3.575 m. Each arm of the building is structurally separated using expansion joints. Fig. 1 shows the schematic representation of the section and plan of building. At plinth level viz. 0.6 m from ground level, longitudinal beams are provided and there are no transverse plinth beams. Foundation is at 1.5 m from ground level. Geometrical details of beams, columns and slabs are provided in Table 1. The longitudinal beams are provided above the windows and not at the floor level, whereas transverse floor beams are provided at floor level. From the sectional drawings, it is learnt that the load bearing masonry and the RC columns (Fig. 1a) were provided to share the floor loads. The grade of concrete used was M20 and grade of steel Fe 415.

Table 1. Sectional properties of beams, columns, and slab.

Member	Size
Longitudinal floor beams	230×600 mm
Transverse floor beams	150×410 mm
External column	150×500 mm
Internal column (plus geometry)	150×300 mm
Longitudinal plinth beams	230×300 mm
Transverse plinth beams	230×450 mm (only at two ends)
Slab	65 mm thick

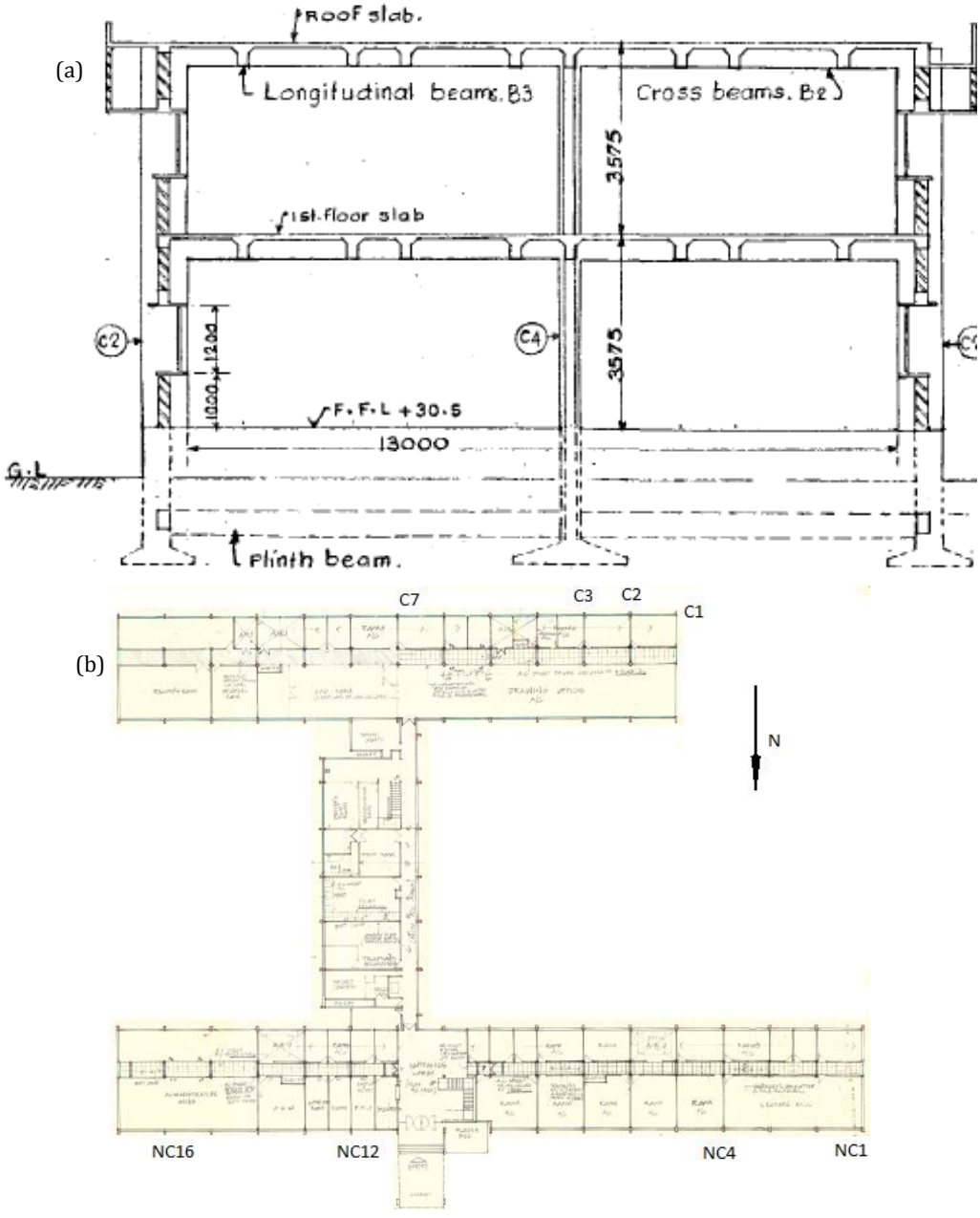

Fig. 1. (continued)

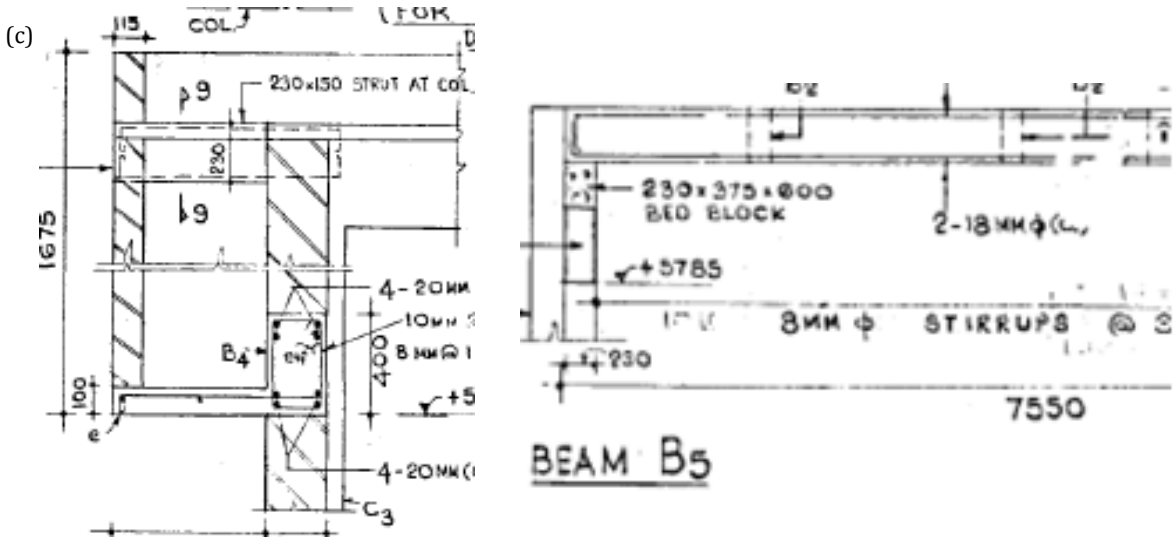

Fig. 1. a) Sectional details; b) Plan of the building; c) Cross-section of floor beams and load-bearing masonry.

3. Assessment Methodologies

3.1. Visual inspection

Visual inspection generally is the primary method used as a first step in assessing the condition of the structure. An expert visual inspection of exposed concrete and masonry helps to detect and define areas of ageing-related distress that result in visible effects on the surface. To begin with, a team of experts inspected both the ground and the first floor of the building. The team evaluated the beams and slabs for explicit visual cracks and other distress in the structural members. During the visual inspection, the nondestructive tests required for precise evaluation of the structures, were also determined.

Fig. 2. Spallation of columns: a) C1; b) C2; c) C3; d) C4.

Fig. 3. Cracks in masonry and sunshades.

The cracks which lead to spallation were more than 2-3 mmand length of 400 mm, whereas hairline cracks of the order of 0.5 mm were also visible. However, initially, cracking and spallation appeared to be due to corrosion, aspect of overloading or settlement of the founding medium etc. could not be overruled. The soil reports from recent adjacent construction site were useful in overruling the issue of settlement of the footing. It was further decided to analyze the frame of the building for the current loading and investigate the condition through non-destructive, semi destructive, electrochemical tests, chemical analyses and X-Ray Diffraction (XRD) etc. as shown in the Table 2. The flow chart depicts the various stages undertaken in the present survey (Fig. 4).

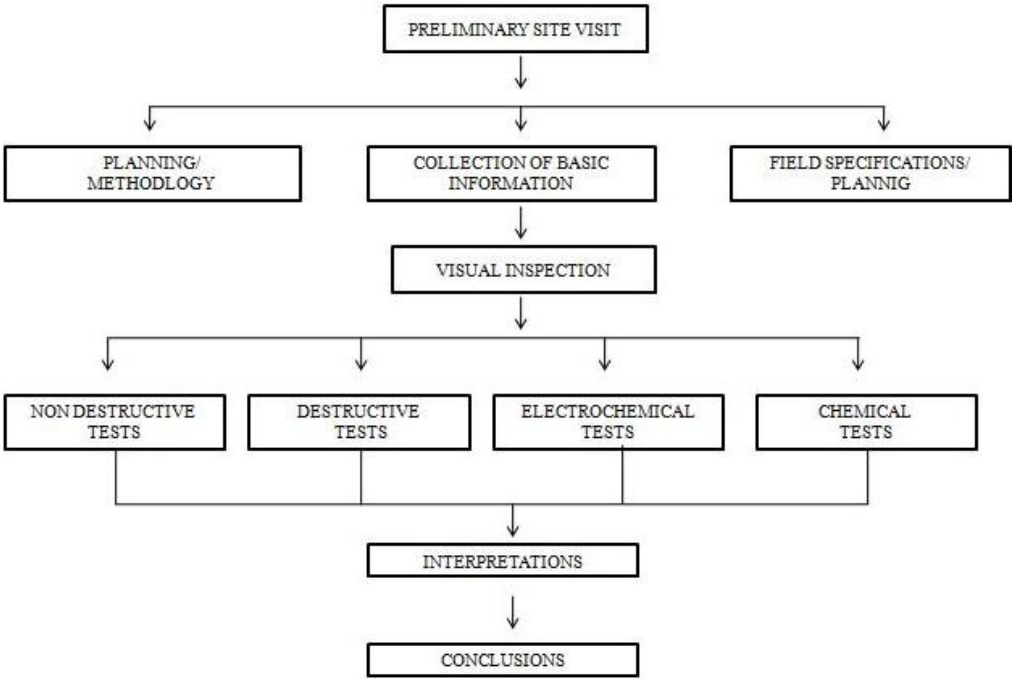

Fig. 4. Flow chart of survey.

Table 2. Condition assessment methods.

Material and characteristic	Column A (*t*)
Concrete / masonry	
General quality	Ultrasonic pulse velocity
Cracking / spalling	Visual inspection, ultrasonic pulse velocity
Strength	Rebound hammer test, ultrasonic pulse velocity
Microbiological assays	Microbially induced corrosion
Concrete reinforcement	
Location of reinforcement	Rebar locator
Corrosion	Visual inspection, electrical resistivity
Concrete durability	pH of the concrete, chloride content detection by titration, carbonation test, RCPT
Micro-chemical analysis	XRD of the concrete samples
Groundwater / soil quality	Chemical analysis, XRF analysis

3.2. Structural analyses

Building is evaluated by modelling and analysis to check the structural capacity of the structure against gravity loading conditions such as dead and live loads. The structural analysis is done using an engineering software .The structure is idealized as a 3D frame, using 3D beam element for columns and beams. Fig. 5 represents the model of the building for the analysis. The member capacity have been calculated using limit state methods given in national code IS 456 (2000), SP-24 (1983) and also ACI 318 (2008). As the structural analysis is to assess the cause of distress, only the dead load and live load as per code IS 875 (1987), and their combination with a partial safety factor of unity is considered.

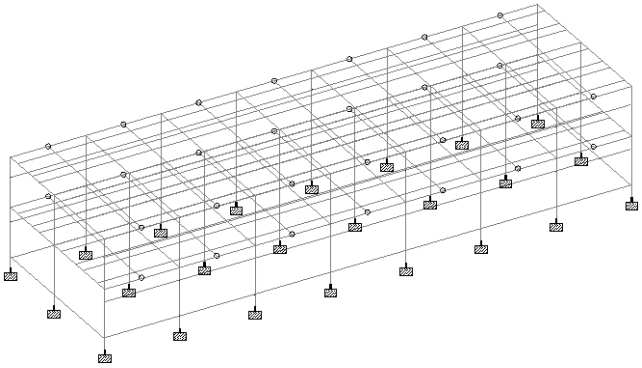

Fig. 5. Partial model of the building.

3.3. Field tests

Locations for performing NDT examinations of rebound hammer, ultrasonic pulse velocity and resistivity were identified on the basis of the environmental exposure conditions viz. coastal environment and distress observed etc. In the overall assessment area totally 26 sampled test points such as external/internal columns and masonry were selected such that the points encompass both the potentially affected areas as well as areas from unaffected portion of the structure, so as to serve as baseline or control.

3.3.1. Rebound hammer test

Schmidt rebound hammer is a simple, handy tool, which can be used to provide a convenient and rapid indication of the compressive strength of concrete. When the plunger of rebound hammer is pressed against the surface of concrete, a spring controlled mass with a constant energy is made to hit concrete surface to rebound back. The extent of rebound, which is a measure of surface hardness, is measured on a graduated scale. This measured value is designated as Rebound Number (rebound index). This is further converted to compressive strength of the material subjected to test. The rebound hammer testing was carried out as per IS 13311 (Part 2) (1992) using Proceq make DIGI-SCHMIDT 2000 concrete test hammer of Model ND/LD. Around each point of observation, nine readings of rebound indices were taken and the average compressive strength was displayed for the point of observation.

3.3.2. Ultrasonic pulse velocity (UPV) test

UPV test is used to measure the velocity of ultrasonic waves inside the concrete to establish the homogeneity and integrity of the concrete, the presence of cracks, voids and other imperfections and the quality of concrete in relation to standard requirement. Ultrasonic instrument used for testing was Proceq Tico ultrasonic instrument which is handy, battery operated and portable instrument. The electronic pulses are generated by the transmitting transducer and collected at the receiving transducer, and the travel time between the two transducers is measured electronically. Grids were made on the selected location, just opposite/adjacent as required to the selected location. The transducer was put on the selected grid on the location and the receiving transducer on the opposite/adjacent grid location after greasing the surface to prevent any air gaps between the testing surface and the transducers. General criterion for concrete quality grading is given in Table 3.

Table 3. Criterion for concrete quality grading as per IS 13311 (Part 1) (1992).

S.No.	Velocity criterion by cross probing (km/sec.)	Concrete quality grading
1	above 4.5	excellent
2	3.5 to 4.5	good
3	3.0 to 3.5	medium
4	below 3.0	doubtful

3.3.3. Resistivity testing of concrete

The electrical resistivity is defined as the ratio between the applied potential and the current circulating between two electrodes providing the arrangement which enables the calculation of the geometrical characteristics. The electrical resistivity is an indirect measurement of the porosity and the connectivity of the pores. It is used to detect wet areas in the concrete and therefore is used to assess the probability or likelihood of corrosion of the reinforcement bar. One of the commercial equipment available for measurement of resistivity of concrete is, Resistivity Meter, which is a four probe device. This is based on the classical four electrode system in which four equally spaced electrodes are electrically connected to the concrete surface. Proceq make Resipod which is a fully integrated 4-point Wenner probe based on Rilem TC 154-E (2000) was used for testing.

Table 4. Interpretation of resistivity results as per RILEM TC 154 (2000).

Resistivity (ρ) range in kΩcm	Risk of corrosion interpretation
< 10	high
10 to 50	moderate
50 to 100	low
> 100	negligible

3.4. Laboratory tests – chemical analysis

At the sites of distress, the spalled concrete was removed and tested for carbonation, pH and chloride penetration. The 6 mm stirrups were fully corroded, while there was a reduction in diameter at the main bar of 22 mm diameter. At one of the columns, the spalled concrete was showing biogenic growth at the inner surface. Hence the sample was tested using microbiological characterization. The topsoil which was covering the columns at the location of distress was also analyzed in the lab using chemical analysis and X-ray Fluorescence. One

of the columns was exposed up to foundation to check the condition below the ground. There was no distress found in the embedded columns and foundation. Water and soil samples were collected from the foundation and tested for sulphates, chlorides or any other harmful chemicals. Spalled, drilled concrete and cored samples were tested for chloride content and pH; further cover concrete was removed for assessing the status for rebars. Rapid chloride penetration test was attempted to determine the permeability of concrete.

3.4.1. Test for chloride content of concrete

The presence of chloride in the concrete is the contributory factor towards corrosion of reinforcement. The chloride content of concrete can be determined by chemical analysis of concrete in the laboratory. The significance of this test is to understand the chloride content present in the concrete and also chloride profiling with depth, to establish whether the source of chloride contamination is internal or external. The chloride content in concrete was determined from broken core samples of the concrete member, in accordance with IS 14959 (Part 2) (2001). As per IS 456, the maximum total Acid Soluble Chloride content for reinforced concrete or plain concrete containing embedded metal is 0.6 kg/m^3. pH was determined using Hanna make HI991300 model portable pH meter.

A colorimetric method based on Collepardi (1995), by spraying Fluoresceine and a Silver Nitrate solution was used to determine the presence of free and bound chloride and its penetration into the concrete structure as it has been generally assumed that free chloride ions can promote the corrosion process of steel reinforcement. In brief, the investigation was carried out at the fractured surfaces of the structure by spraying the Fluoresceine solution (1g/L in a 70% solution of ethyl alcohol in water) followed by Silver Nitrate (0.1mol/l) aqueous solution. A dark pink coloration indicated presence of free chloride areas and a dark brown coloration indicated bound chloride zone on the grey concrete (Fig. 6). This process was also adopted on a fractured core sample extracted from the structure, wherein the depth of free chloride penetration was indicated by a color change with a clear demarcation till the region of bound chloride region.

Fig. 6. Colorimetric method to check free and bound chloride on the exposed structural member.

3.4.2. Rapid chloride penetration test(RCPT)

A cylindrical core specimen (200×100 mm) was typically cut as a slice (50×100 mm) and used for this test. The RCPT apparatus consists of two reservoirs. The specimen was fixed between two reservoirs using an epoxy bonding agent to make the test setup leak proof. One reservoir (connected to the positive terminal of the Direct current (DC) source) was filled with 0.3N NaOH solution and the other reservoir (connected to the negative terminal of the DC source) with 3% NaCl solution. The terminals were then connected to the 60 V DC power supply and the current reading in mA was recorded for every half an hour up to 6 hrs. The total charge passed during this period was calculated in terms of coulombs using the trapezoidal rule as given in the ASTM C1202 (2019).

3.4.3. Carbonation

The carbonation test was carried out as per RILEM CPC-18 (1988). The reduction of the pH value could be made visible by applying a 1% phenolphthalein solution to a freshly fractured surface of concrete. The non-carbonated areas turn red or purple while carbonated areas remain colorless. The phenolphthalein solution was sprayed on the freshly cored concrete surface and the color change was observed (Fig. 7).

3.4.4. Microbiological assays

The spalled concrete from C3 column had a pale yellow color deposition (Fig. 8). The deposit was sliced and observed under a light microscope for microscopic structures. Fungal cells in spalled concrete and soil re-

sembled of Gaeumannomycella / Gaeumannomyces sp. and hyphopodia and also sulphur reducing bacteria. This was confirmed by using the deposit as an inoculum for microbial enrichment in Saboraud dextrose broth and Luria-Bertani broth. Sulphur was not present in X-Ray fluorescence (XRF) analysis of the deposited sample.

Fig. 7. Concrete carbonation tests on the fractured structural member, cored member and checking for the corrosion of rebar.

Fig. 8. Biogenic growth at the inner face of the column.

3.4.5. X-ray diffraction (XRD) of concrete samples

XRD data were acquired on Intel make machine (Model - Equinox 2000) equipped with Gas Detection Cell (Argon and Ethan) detector and intensity measurements were carried out using germanium mono-chromated Cu-Kα radiation (λ=1.789 A^0) in asymmetric acquisition mode. XRD involves directing an incident wave into a material and recording outgoing diffracted wave direction and intensity using a detector. Scattered waves emitted from an atom of different type and position, interface constructively or destructively along different paths. The crystal structure of a material is related to this diffraction pattern. By scanning, a sample in 2θ range, all possible diffraction directions is obtained. The crystal phases of crushed concrete specimen were determined by correlating the change in intensity in the field of 10-80° of 2θ. Crystalline phases identified from the standard database, JCPDS (1985) and literature.

4. Results and Discussion

4.1. Visual inspection

Though cracking was not visible at first, except for in few columns in the southern block, close inspection revealed hairline cracks and also signs of repairs previously carried out in several columns. Except for the south block, plinth protection and drain covered the columns all around the periphery. The south block columns showed distress to a height of 0.8 m from the ground level. Organic soil was observed to cover this particular height of the column for quite some duration and distress became visible on removing the soil cover. Roughcast plastered external masonry, though appeared intact outside; cracking was seen at the inner surface. There was visible distress in masonry and window panes associated with the columns. There were no evident signs of distress in the internal beams and columns.

4.2. Structural analyses

The external columns were found to be sway columns with a slenderness ratio exceeds 22 in both directions, according to ACI 318 (2008). Axial loads in the columns were exceeding the Euler critical load applying the stiffness variation in columns due to cracking, creep and column non-linearity (Figs. 9-11). Hence peripheral columns (150×500 mm) were failing due to instability and buckling.

4.3. Nondestructive tests

Rebound hammer and UPV were resorted to identify the condition of masonry, initially, at areas where there were no visible defects (Table 5). With these readings as reference, the tests were conducted at areas where hairline cracks were visible in masonry. The range of UPV at good locations was 3450-4450 m/s using the direct transmission method and 2880-3220 m/s using the surface transmission method. At regions where cracking was seen, the UPV dipped to 2600 m/s which show degradation. The compressive strength obtained from rebound hammer, both for concrete columns /beams and masonry were in the range 35-45 N/mm^2.

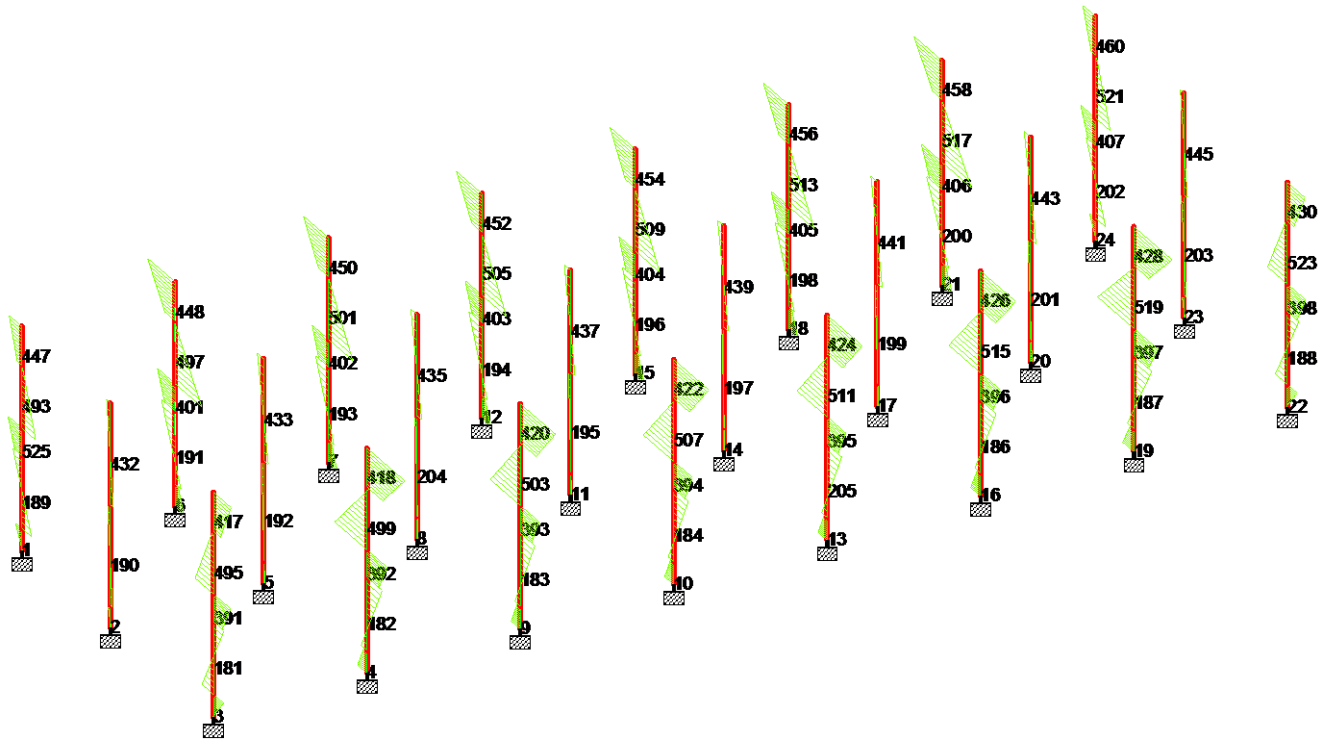

Fig. 9. Column bending moment along the major axis due to static loads.

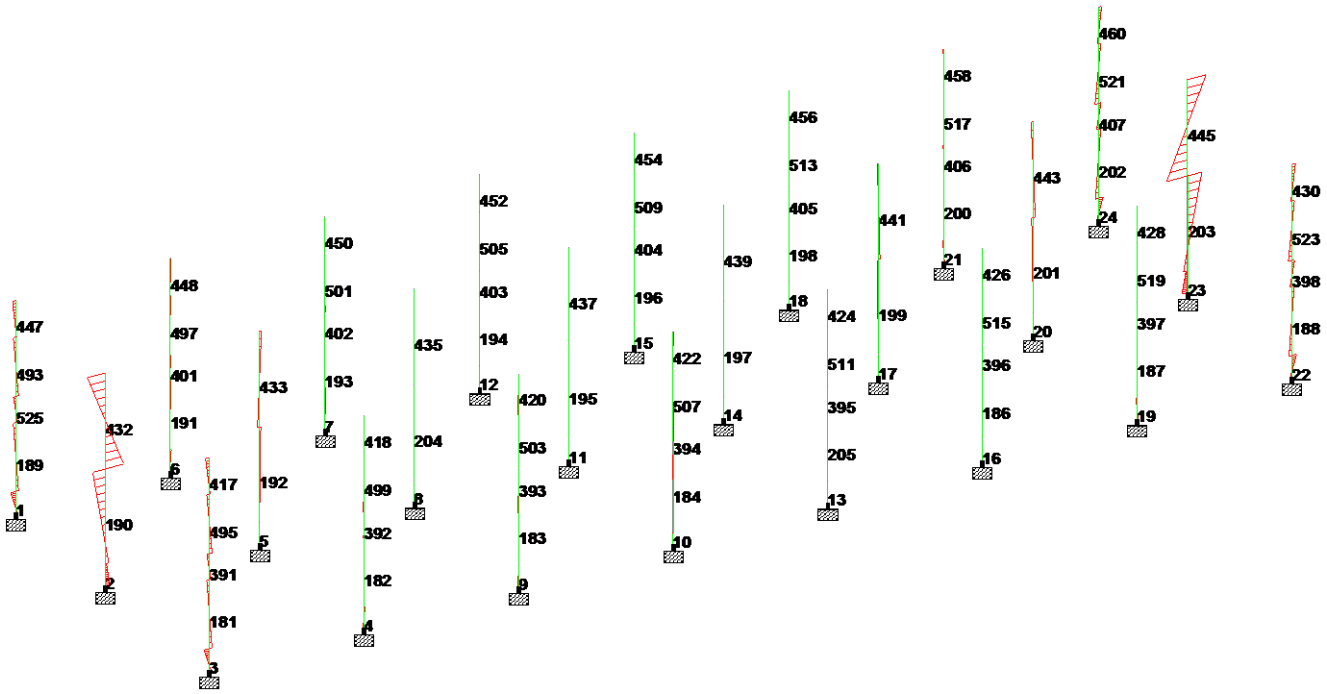

Fig. 10. Column bending moment along the minor axis due to static loads.

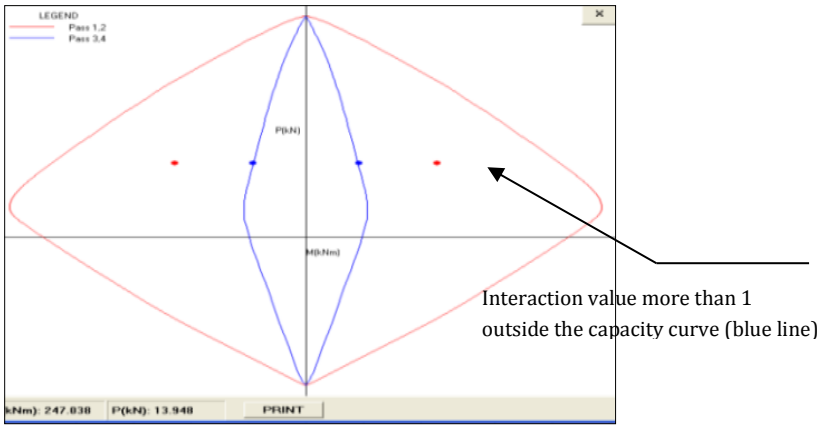

Fig. 11. Interaction chart by using the additional moment method as per ACI 318 (2008).

The external columns were further tested after validating the healthiness of columns inside the building. The columns showed reduced UPV values in the range of 2320 m/s near the distress, 4700 m/s at -0.9 m from ground level, 4660 & 4460 m/s at -0.6 m and -0.3 m levels respectively. Just above the distressed area also the UPV was as high as 4240 m/s. These values prove that the distress is highly localized. The distressed area was dry hence half-cell potential measurements when tried gave only positive potentials. Even resistivity measured in the distressed columns showed high values. But below ground, the resistivity dipped to 33-67 K ohm-cm, which is due to moisture in the soil. UPV conducted on external columns at the north block rendered values of 4000-3500 m/s, suddenly dipping to 3300 m/s at the hairline cracks.

Table 5. Results of the nondestructive tests.

S.No.	Location	Rebound hammer values (N/mm^2)	UPV (m/sec)
1	C2 column +0.6 m from crack	40.0	3820
2	C3 column +0.3 m from crack	40.0	4240
3	C3 column near crack	38.8	0-2320
4	C3 column-0.9m from crack	44.3	4700
5	C3 column- 0.6m from crack	39.0	4660
6	C3 column -0.3m from crack	43.3	4460

Table 6. Chloride and sulphate in founding medium.

Ion	Concentration (%)
Chloride	0.0055
Sulfate	0.0066

Table 7. Elemental composition in founding medium-XRF.

S.No	Element	Concentration (%)
1	Al	3.91 ±0.01
2	Si	24.17 ±0.12
3	Ca	3.06 ±0.18
4	Fe	3.26 ±0.12

4.4. Chemical analysis

Tables 6 and 7 gives chloride, sulphate and elements in soil. Table 8 gives analysis results for carbonation, chloride penetration and pH of spalled concrete samples. Chemical analysis showed high chloride content on an average 1.4 kg/m^3 in external concrete columns and 0.9 kg/m^3 at internal columns, which was almost uniform with depth. Carbonation levels at ground level of external columns were very high whereas carbonation at inner columns and beams and upper elevations of external columns was nil. The total charge passed through the concrete specimen in RCPT was 5000 Coulombs which shows high chloride ion penetrability of concrete.

Chloride ions can get introduced into concrete through raw materials such as aggregate, mixing water (internal chloride) and admixtures or from chloride sources in the service environment (intruded chloride). Calcium chloride was prevalent as an accelerating admixture in concrete in 1970s as given in Clarke (2009) to increase the rate of early strength development, reduce the setting time or to increase the production rate in precast industry according to Chen (2017). When concrete is contaminated as a result of the use of calcium chloride, it is identifiable by an even distribution of the chloride content between 0.5 and 1% by mass of cement as per Brueckner et al. (2017) and Kim et al. (2018) (as recommended $CaCl_2$ was less than 1.5%). When concrete is contaminated due to external sources the chloride profile decreases from the face of exposure to interior. Gebregziabhier (2008) explains that the internal chloride ions affect the hydration process and hydration products of cementitious materials as they get introduced in fresh state, while the external chloride alters the pore structure and solid/ liquid phase composition within concrete. Once inside concrete, chloride assumes any three states, free chloride in bulk pore solution, physically adsorbed chloride on the surface of hydration products or chemically bound chloride by solid phase. The chemically bound chloride results in decrease of porosity by formation of Friedel's salt ($3CaO\_Al_2O_3\_CaCl_2\_10H_2O$) and Kuzel's salt ($3CaO\_Al_2O_3\_0.5CaCl_2\_0.5CaSO_4\_10H_2O$). With carbonation, there is decrease in concrete alkalinity from pH 12.5–13 towards pH 9 and during this process bound chlorides are released back into solution, which increases the free chloride content over time (Eq. (1)). Ettringite also does not exist in severely carbonated concrete as its stability is also pH dependent.

$$3CaO.Al_2O_3.CaCl_2.10H_2O + 3CO_2 \rightarrow 3CaCO_3 + 2Al(OH)_3 + CaCl_2 + 7H_2O \quad (1)$$

So in carbonated environment the carbonation progresses to the depth of the reinforcement and the protective layer on the steel destabilizes causing initiation of corrosion in the presence of oxygen and moisture or the release of chlorides into the pore solution may exceed the critical chloride threshold and cause corrosion before the carbonation front reaches the reinforcement. Corrosion of reinforcement causes the formation of voluminous reaction products which can cause spalling and delamination of the concrete cover. According to Kim et al, in cement the content of C_3A and C_4AF dominates the chemical binding of chloride ions, while C_3S and C_2S dominates physical binding. Hence threshold chloride content can vary with type of cement, depending on the C_3A and C_4AF content. The reaction of C_3A with chloride forms Friedel's salt, which removes free chlorides from the pore solution and thus not participate in the corrosion process. Thus high concentration of C_3A is inhibits chloride-induced corrosion of steel in concrete. And it is also seen that internal chloride showed higher chloride threshold than external chloride, as lesser amount of free chloride participate in the corrosion process, due to chloride binding in the initial hydration stage.

4.5. X-ray diffraction of the concrete samples

XRD of fresh concrete usually shows (Fig. 12) the crystalline peaks of hydration products, Calcium hydroxide, gypsum, ettringite, continuous bumps of calcium silicate hydrate gels, calcium carbonate etc. and quartz phase from aggregate and cement. In the sample, calcium hydroxide or Portlandite phase at 2θ angle of 18 & 34° were missing, which were replaced by peaks at 2θ angle of 23-25°,26-27°,39-40°, 78°, as calcite/vaterite and aragonite according to Stutzman (2010), the polymorphs of calcium carbonate. Calcite which is in abundance in the 40 mm layer of the concrete is the most stable polymorph. Vaterite is in concrete due to the high ambient temperature at site and aragonite, due to the presence of chloride as given in Ramakrishna et al. (2016). Other crystalline products identified were bassanite ($CaSO_4.5\ H_2O$) (at 2θ angle of 20.72°, 23.23°, 29.7°, 42.45°), and langbeinite (potassium magnesium sulphate etc.) (at 2θ angle of 21.92°, 25.39°, 26.93°, 31.2°, 39.55°, 41.69°, 43.1°).These are products formed due to the instability of gypsum and ettringite in carbonated environment along with high temperatures. Quartz phase from 2θ angle of 20.85°, 26.65°, 36.54°, 39.46°, 50.14°, 60° and 68° were evident in some samples of external/internal columns, but not in all which shows some ageing. Calcium monosulphates (2θ angle of 10.2°) and Friedel salt (2θ angle of 11.05°) also appeared in some inner layers of samples as given in Hashimoto et al. (2012), Fujiwara et al. (1992), Florea et al. (2012), and

Suryavanshi et al. (1996). The peaks at 2θ angle of 13-14° indicate free chloride. Ettringite peaks at 2θ angle of 23.5° were seen in the sample of C3 column, having biogenic growth.

Table 8. Chloride content and pH of concrete.

S.No.	Sample no.	Average chloride	Average pH	Estimated depth of carbonation
1	C2 + 0.8 lvl	1.239	8.955	40-50 mm
2	C3 + 0.8 lvl	1.415	10.805	40-50 mm
3	C7 + 0.8 lvl	1.365	10.115	
4	C2 + 4.75 m	0.885	10.40	
5	C3 + 4.75 m	1.504	11.58	
6	C7 + 4.75 m	1.482	10.87	
7	NC1 + 0.8 lvl	1.4891	10.29	20 mm
8	NC4 + 0.8 lvl	1.5147	11.46	20 mm
9	NC12 + 0.8 lvl	1.5051	11.60	15 mm
10	NC16 0lvl	0.4378	10.79	40 mm
11	NC4 + 1.75 m	0.806		0
12	NC4 + 4.75 m	0.993		0
13	NC16 + 4.75 m	0.250		0
14	NC16 + 1.75 m	1.613		2 mm
15	NC12 + 1.75 m	2.995		0 mm
16	Internal beam 1	0.791	11.52	0 mm
17	Internal beam 2	0.594	11.28	0 mm

5. Conclusions

- While checking the capacity of the structure for unfactored static load combination peripheral columns (150×500 mm) were found to be failing by instability and buckling, considering age related degradation in stiffness as per ACI 318, which leads to structural cracking of the columns. Nonlinear static pushover analysis is suggested for further structural assessment.
- Nondestructive testing validates the visual inspections that the external columns are cracking locally just above the ground. The integrity of columns just above and below this localized region was good.
- Chemical analysis showed high chloride content (1.4 kg/m^3) in external concrete columns and 0.9 kg/m^3 at internal columns. As the chloride content from surface to interior was uniform, the source of chloride is assessed to be internal, that would have admixed during hydration (say $CaCl_2$ of less than 1%). Concrete core from an inner column showed evidence of bound chloride from chemical analysis and in XRD, which explained the absence of corrosion in the internal elements, even though total chloride content was exceeding the threshold value (of 0.6 kg/m^3).
- The grade of OPC cements used in the 1970's contained high C_3A content of 10% and more as per internal quality reports and Shetty (1988), which chemically bonded chloride to Calcium chloroaluminate (Friedel salt). But XRD of spalled concrete from external columns were not showing Friedel salt peaks. The outer columns were heavily carbonated, and at high carbonation levels the Friedel salt is unstable hence breaks into free chloride which corrodes the rebars.
- The reason for higher carbonation at the lower levels of column is the structural cracking and the conjugal higher permeability based on Saeki (2002). It can be inferred that, structural instability in the columns lead to the cracks, which further increased the carbonation release of free chloride leading to corrosion of rebars, expansion, and spallation.

From the above it is inferred that, the direct cause of distress could not be attributed to a single cause since many factors co-exist such as cracking, carbonation and presence of chloride. These factors are interrelated.

Ina holistic perspective, it is concluded that, only external columns got cracked due to local effects, and internal structural elements were healthy. Considering the level of structural degradation of columns for continuing the functional requirement as per the current national standards and deterioration of material property in steel and concrete, appropriate measure for retrofit needs to be evolved, based on further structural assessment.

Acknowledgements

Authors are obliged to the labs of WSCD (BARCF), HSEG and XSCGS of Indira Gandhi Centre for Atomic Research for conducting tests for chloride, sulphates, microbiological assays, XRF and XRD which helped in the interpretation of the results.

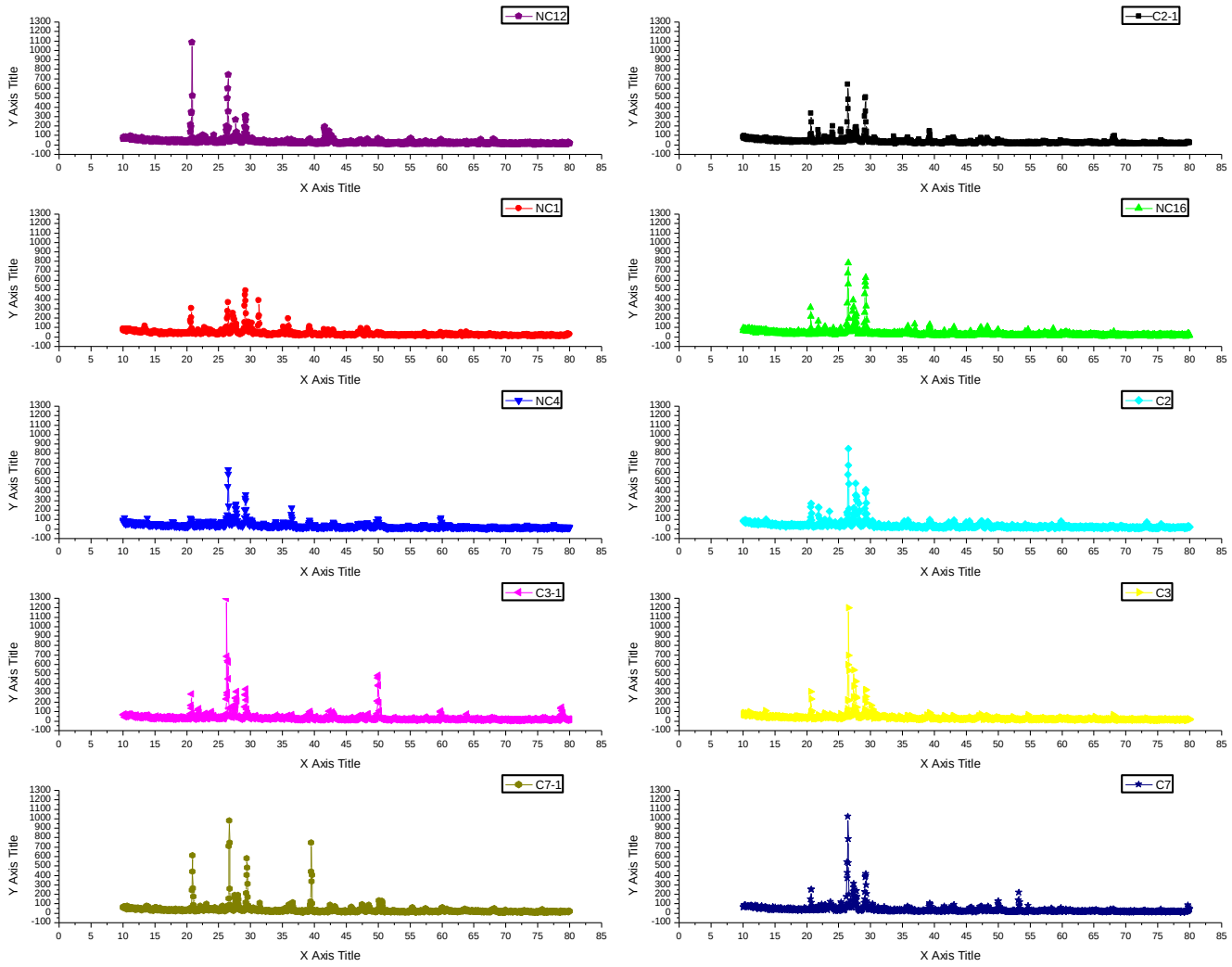

Fig. 12. XRD results the concrete samples.

Funding

The authors received no financial support for the research, authorship, and/or publication of this manuscript.

Conflict of Interest

The authors declared no potential conflicts of interest with respect to the research, authorship, and/or publication of this manuscript.

References

ACI 318 (2008). Building Code Requirement for Structural Concrete. American Concrete Institute, Farmington Hills, Michigan, USA.

ACI 365.1R (2000). Service Life Prediction-State of Art Report. American Concrete Institute, Farmington Hills, Michigan, USA.

Ahmad S (2003). Reinforcement corrosion in concrete structures, its monitoring and service life prediction – a review. *Cement & Concrete Composites*, 25(4-5), 459–471.

ASTM C1202 (2019). Standard Test Method for Electrical Indication of Concrete's Ability to Resist Chloride Ion Penetration. American Society for Testing and Materials, West Conshohocken, PA, USA.

Brueckner R, Lambert P (2017). Unexpected effects of historic concrete innovations. *International Journal of Heritage Architecture*, 1(4), 549-563.

Chen MC, Restrepo JI (2021). Service-life performance case studies of underground reinforced concrete utility vaults. *Journal of Performance of Constructed Facilities*, 04021006.

Chilakala R, Thenepalli T, Huh JH, Ahn JW (2016). Preparation of needle-like aragonite precipitated calcium carbonate (PCC) from dolomite by carbonation method. *Journal of the Korean Ceramic Society*, 53(1), 7-12.

Clarke JL (2009). Historical approaches to the design of concrete buildings and structures. Technical Report 70, Concrete Society, Camberley, Surrey, UK.

Collepardi M (1995). Quick method to determine free and bound chlorides in concrete. *1st RILEM workshop on Chloride Penetration into Concrete*, St Rémy lès Chevreuse, France, 10-16.

Dhawan S, Bhalla S, Bhattacharjee B (2014). Reinforcement corrosion in concrete structures and service life predictions – A review. *9th International Symposium on Advanced Science and Technology in Experimental Mechanics*, New Delhi, India, 1-6.

Florea MVA, Brouwers HJH (2012). Chloride binding related to hydration products - Part I: Ordinary portland cement. *Cement and Concrete Research*, 42, 282–290.

Fujiwara Y, Maruya T, Owaki E (1992). Degradation of concrete buried in soil with saline groundwater. *Nuclear Engineering and Design*, 138,143-150.

Gebregziabhier TT (2008). Durability problems of 20th century reinforced concrete heritage structures and their restorations. *M.Sc. thesis*, Barcelona School of Civil Engineering, Barcelona, Spain.

Hashimoto K, Yokota H, Sato Y, Sugiyama T (2012). Chloride ion binding behaviour of deicing salts under freeze-thaw environment. *2nd International Conference of Microstructural Durability of Concrete Composites*, Amsterdam, Netherlands, 622-629.

IS 13311 (Part 1) (1992). Methods of Non–destructive Testing of Concrete: Part 1 Ultrasonic Pulse Velocity. Bureau of Indian Standards, New Delhi, India.

IS 13311 (Part 2) (1992). Methods of Non–destructive Testing of Concrete: Part 2 Rebound Hammer. Bureau of Indian Standards, New Delhi, India.

IS 456 (2000). Plain and Reinforced Concrete - Code of Practice. Bureau of Indian Standards, New Delhi, India.

IS 875 Part –I & II (1987). Design Loads (other than earthquake) for Buildings and Structures. Bureau of Indian standards, New Delhi, India.

IS14959 (Part 2) (2001). Determination of Water Soluble and Acid Soluble Chlorides in Mortar and Concrete – Method of Test – Part 2: Hardened Mortar and Concrete. Bureau of Indian Standards, New Delhi, India.

Kim MJ, Ann KY (2018). Corrosion Risk of Reinforced Concrete Structure Arising from Internal and External Chloride. *Advances in Materials Science and Engineering,* 2018, 1-7.

Natesan M, Venkatachari G, Palaniswamy N (2005). Corrosivity and durability map of India. Corrosion Science and Engineering Division, Central Electrochemical Research Institute, Karaikudi, lndia. https://krc.cecri.res.in

Qazweeni JA, Daoud OK (1991). Concrete deterioration in a 20-year-old structure in Kuwait. *Cement and Concrete Research*, 21, 1155-1164.

RILEM CPC-18 (1988). Measurement of Hardened Concrete Carbonation Depth. RILEM Publications SARL, 21(126), 453-455, RILEM, Marne la Vallée Cedex 2, France.

Rilem Tc 154-E (2000). Electrochemical Techniques for Measuring Metallic Corrosion. RILEM Publications SARL, 36(261), 461–471, RILEM, Marne la Vallée Cedex 2, France.

Saeki T (2002). Effect of carbonation on chloride penetration in concrete. *3rd RILEM workshop on Testing and Modelling the Chloride Ingress into Concrete*, Madrid, Spain, 381-394.

Shetty MS (1988). Concrete Technology. S.Chand & Co., India.

SP 24 (1983). Explanatory Handbook on Indian Standard Code of Practice for Plain and Reinforced Concrete (IS 456:1978). Bureau of Indian standards, New Delhi, India.

Standard X-Ray Diffraction Powder Pattern (1985). Joint Committee of Powder Diffraction Standards (JCPDS). American Chemical Society, Washington, DC, USA.

Stutzman P (2010). Direct Determination of Phases in Portland Cements by Quantitative X-Ray Powder Diffraction. Technical Note (NIST TN), National Institute of Standards and Technology, Gaithersburg, MD.

Suryavanshi AK, Scantlebury JD, Lyon SB (1996). Mechanism of Friedel's salt formation in cement rich in tri-calcium aluminate. *Cement and Concrete Research*, 26(5), 717-727.